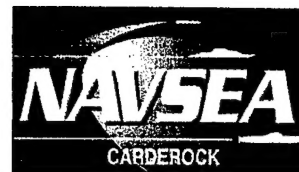


**Carderock Division  
Naval Surface Warfare Center**

9500 MacArthur Boulevard  
West Bethesda, Maryland 20817-5700



NSWCCD-50-TR-2001/037

JULY 2001

Hydromechanics Directorate

**Wavenumber-Frequency Characteristics of  
Partial Wall Pressures from Large Eddy Simulations  
of a Turbulent Channel Flow**

by  
Peter A. Chang, III



20010720 074



Approved for public release; distribution is unlimited

REPORT DOCUMENTATION PAGE			Form Approved OMB No. 0704-0188	
Public reporting burden for this collection of information is estimated to average 1 hour per response, including the time for reviewing instructions, searching existing data sources, gathering and maintaining the data needed, and completing and reviewing the collection of information. Send comments regarding this burden estimate or any other aspect of this collection of information, including suggestions for reducing this burden, to Washington Headquarters services, Directorate for Information Operations and Reports, 1215 Jefferson Davis Highway, Suite 1204, Arlington, VA 22202-4302, and to the Office of Management and Budget, Paperwork Reduction Project (0704-0188), Washington, DC 20503.				
1. AGENCY USE ONLY (Leave blank)		2. REPORT DATE July 2001		3. REPORT TYPE AND DATES COVERED Formal Report
4. TITLE AND SUBTITLE Wavenumber-Frequency Characteristics of Partial Wall Pressures from Large Eddy Simulations of a Turbulent Channel Flow			5. FUNDING NUMBERS N0001499WX20508 Program Element 0601153	
6. AUTHOR(S) Peter A Chang, III				
7. PERFORMING ORGANIZATION NAME(S) AND ADDRESS(ES) Naval Surface Warfare Center Carderock Division 9500 MacArthur Boulevard West Bethesda, MD 20817-5700			8. PERFORMING ORGANIZATION REPORT NUMBER NSWCCD-50-TR—2001/037	
9. SPONSORING/MONITORING AGENCY NAME(S) AND ADDRESS(ES) Office of Naval Research, Code 333 800 N. Quincy St. Arlington, VA 22201			10. SPONSORING/MONITORING AGENCY REPORT NUMBER	
11. SUPPLEMENTARY NOTES				
12a. DISTRIBUTION/AVAILABILITY STATEMENT Approved for public release; distribution is unlimited.			12b. DISTRIBUTION CODE	
13. ABSTRACT (Maximum 200 words)  This report documents, for the first time, the wavenumber and frequency characteristics of the mean-shear (MS) and turbulence-turbulence (TT) partial wall pressures. Results show that both the TT and MS pressures are important for the convective pressures, but that the TT pressure dominates in the subconvective wavenumber range. At low frequencies both the buffer layer and logarithmic region contribute significantly to the MS convective pressure; at higher frequencies the buffer layer is dominant. The partial pressures were obtained from two large eddy simulations (LES) of a fully-developed turbulent channel flow ; they were computed from the TT and MS source terms from four regions of the channel (viscous shear layer, buffer region, logarithmic region and upper channel). The Reynolds number based on momentum thickness and shear velocity was 24; based on channel half-width and shear velocity, 171. The non-linear terms in the simulation, as well as those pressure source terms were dealiased using the 2/3 rule. The first simulation, LES8, used the rotational form of the nonlinear terms, whereas the second simulation, LES9, used the skew-symmetric form. Significant differences between the two simulations appear only in the subconvective wavenumber range for the TT spectra that has been integrated over the entire channel, pointing to the fact that the skew-symmetric form, while more expensive, computationally, is more accurate.				
14. SUBJECT TERMS wall pressure fluctuations hydroacoustics subconvective pressure			15. NUMBER OF PAGES 41	
			16. PRICE CODE	
17. SECURITY CLASSIFICATION OF REPORT UNCLASSIFIED			18. SECURITY CLASSIFICATION OF THIS PAGE UNCLASSIFIED	
19. SECURITY CLASSIFICATION OF ABSTRACT UNCLASSIFIED			20. LIMITATION OF ABSTRACT SAR	

## CONTENTS

NOMENCLATURE . . . . .	v
ABBREVIATIONS . . . . .	vi
COVER ILLUSTRATION . . . . .	vi
EXECUTIVE SUMMARY . . . . .	1
ADMINISTRATIVE INFORMATION . . . . .	1
ACKNOWLEDGEMENTS . . . . .	2
INTRODUCTION . . . . .	2
MATHEMATICAL FORMULATION . . . . .	3
Computation of partial pressures . . . . .	5
Computation of partial pressure spectra . . . . .	6
PRESENTATION OF RESULTS . . . . .	8
Mean velocity and turbulence intensity profiles . . . . .	8
Mean square variation of pressure with time . . . . .	8
Point frequency spectra . . . . .	9
$k_x - \omega$ spectra— R1234 . . . . .	15
Partial MS and TT pressures — R1234 . . . . .	15
Partial pressures from regions of channel . . . . .	23
One-dimensional spectra of partial pressures . . . . .	23
Two-dimensional $k_x - \omega$ spectra of partial pressures . . . . .	23
Convection velocities . . . . .	23
Constant- $\omega$ cuts of $k_x - \omega$ spectra of partial pressures . . . . .	34
Comparison to semi-empirical formulations . . . . .	37
CONCLUSIONS . . . . .	37
REFERENCES . . . . .	39

## FIGURES

	Page
1. Viscous-scaled mean velocity profiles . . . . .	9
2. Turbulence intensity profiles . . . . .	10
3. Temporal variation of m.s. (mean-square) TT, MS and total pressures . . . . .	11
4. Inner- and outer-scaled point frequency spectra . . . . .	13
5. Two-dimensional contour plots of $k_x - \omega$ spectra for $\pi^{Tot}(R1234)$ . . . . .	14
6. Constant frequency cuts of $k_x - \omega$ spectra of total pressures from entire channel (R1234) . . . . .	17
7. One-dimensional spectra of partial pressures for sources integrated over entire channel (R1234) . . . . .	18

8. Two-dimensional contour plots of $k_x - \omega$ spectra from LES8 for all regions (R1234) . . . . .	19
9. Two-dimensional contour plots of $k_x - \omega$ spectra from LES9 for all regions (R1234) . . . . .	20
10. Constant frequency cuts of $k_x - \omega$ spectra of partial pressures from LES8 for all regions (R1234) . . . . .	21
11. Constant frequency cuts of $k_x - \omega$ spectra of partial pressures from LES9 for all regions (R1234) . . . . .	22
12. One-dimensional spectra of $\pi^{MS}$ from LES8 . . . . .	25
13. One-dimensional spectra of $\pi^{TT}$ from LES8 . . . . .	26
14. Two-dimensional contour plots of $k_x - \omega$ spectra of $\pi^{MS}$ from LES8 . .	27
15. Two-dimensional contour plots of $k_x - \omega$ spectra of $\pi^{MS}$ from LES8 . .	28
16. Two-dimensional contour plots of $k_x - \omega$ spectra of $\pi^{TT}$ from LES8 . .	29
17. Two-dimensional contour plots of $k_x - \omega$ spectra of $\pi^{TT}$ from LES8 . .	30
18. Two-dimensional contour plots of $k_x - \omega$ spectra of $\pi^{TT}$ from LES9 . .	31
19. Two-dimensional contour plots of $k_x - \omega$ spectra of $\pi^{TT}$ from LES9 . .	32
20. Convection velocities from peak of $k_x - \omega$ spectra from LES8 . . . . .	33
21. Constant frequency cuts of $k_x - \omega$ spectra of MS partial pressures from four regions of the channel . . . . .	35
22. Constant frequency cuts of $k_x - \omega$ spectra of TT partial pressures from four regions of the channel . . . . .	36
23. Comparison to Chase . . . . .	38

## TABLES

	Page
1. Regions of the channel . . . . .	5
2. Frequency spectra parameters . . . . .	12

## NOMENCLATURE

$G$	Green's function
$\mathbf{h}$	Advective term in Navier-Stokes equations, $m/sec^2$
$k$	One-dimensional wavenumber, $1/m$
$K$	Planar wavenumber magnitude $= \sqrt{k_x^2 + k_z^2}$ , $1/m$
$\mathbf{K}$	Planar wavenumber vector, $1/m$
$N_t$	Number of points in a sampling period
$p$	Dynamic pressure, $kg/(m \cdot sec^2)$
$P$	Computed pressure, $kg/(m \cdot sec^2)$
$r$	Region number
$Re_\tau$	Reynolds number based on $u_\tau, \delta$
$Re_o$	Reynolds number based on $U_o, \delta$
$Re_{\delta^*}$	Reynolds number based on $u_\tau, \delta^*$
$t$	Time, $sec$
$T_{ij}$	Pressure source term $ij$ , $sec^{-2}$
$\mathbf{u}$	Velocity vector, $m/sec$
$u, v, w$	Streamwise, wall-normal, and spanwise velocities, respectively, $m/sec$
$u_\tau$	Friction velocity, $m/sec$
$U_\ell$	Laminar centerline velocity, $m/sec$
$U_o$	For TCF the turbulent centerline velocity, for TBL, the outer flow velocity, $m/sec$
$u^+$	Time- and space-averaged streamwise velocity normalized by $u_\tau$
$u_\tau$	Friction velocity, $= \sqrt{\tau_w/\rho}$
$x, y, z$	Streamwise, wall-normal and spanwise coordinates, respectively, $m$
$y^+$	Wall-normal distance in wall units, $= yu_\tau/\nu$
$\alpha, \beta$	Angle, $radians$
$\delta$	Channel half-width, $m$
$\delta^*$	Momentum thickness, $m$
$\Delta$	Divergence operator, $m^{-1}$
$\nu$	Kinematic viscosity, $m^2/sec$
$\omega$	Radian frequency, $1/sec$
$\Phi$	Two-dimensional pressure spectra
$\Pi_{ij}(Rr)$	Partial pressure due to term $ij$ and region $r$ , $kg/(m \cdot sec^2)$
$\Psi$	Three-dimensional pressure spectra
$\rho$	Density, $kg/m^3$
$\tau_w$	Wall shear stress, $kg/(m \cdot sec^2)$
$\omega_c^+$	Radian frequency at which 1/2 of the convective ridge is resolved, $rads$
$\omega^+$	Radian frequency normalized by viscous units $\equiv \omega\delta^+/u_\tau$

## ABBREVIATIONS

CFL	Courant-Friedrichs-Lewy
CM	Choi and Moin
DNS	Direct numerical simulation
FT	Fourier transform
IFT	Inverse Fourier transform
LES	Large eddy simulation
MHz	megaHertz
m.s.	Mean-square
MS	Mean-shear
N-S	Navier-Stokes
RANS	Reynolds-averaged Navier-Stokes
SGI	Silicon Graphics
SGS	Sub-grid scale
TBL	Turbulent boundary layer
TCF	Turbulent channel flow
TT	Turbulence-turbulence
WPF	Wall pressure fluctuation

## COVER ILLUSTRATION

Pseudo-color image of wall pressure due to mean-shear (MS) pressure from sources in the entire channel. Red indicates regions of positive pressure, blue, negative pressure. Image was extracted from animations of wall pressure generated for MS and turbulence-turbulence (TT) sources from individual regions of the channel. Pressures generated from the channel flow simulations are documented in this report.

## ABSTRACT

*This report documents, for the first time, the wavenumber and frequency characteristics of the mean-shear (MS) and turbulence-turbulence (TT) partial wall pressures. Results show that both the TT and MS pressures are important for the convective pressures, but that the TT pressure dominates in the subconvective wavenumber range. At low frequencies both the buffer layer and logarithmic region contribute significantly to the MS convective pressure; at higher frequencies the buffer layer is dominant. The partial pressures were obtained from two large eddy simulations (LES) of a fully-developed turbulent channel flow; they were computed from the TT and MS source terms from four regions of the channel (viscous shear layer, buffer layer, logarithmic region and upper channel). The Reynolds number for the simulations was,  $Re_{\delta^*} = u_{\tau}\delta^*/\nu \approx 24$  ( $Re_{\tau} = 171$ ); the non-linear terms in the simulation, as well as those pressure source terms were dealiased using the 2/3 rule. The first simulation, LES8, used the rotational form of the nonlinear terms, whereas the second simulation, LES9, used the skew-symmetric form. Significant differences between the two simulations appear only in the subconvective wavenumber range for the TT spectra that has been integrated over the entire channel, pointing to the fact that the skew-symmetric form, while more expensive, computationally, is more accurate.*

## EXECUTIVE SUMMARY

This work is part of an effort to develop a hybrid RANS/Analytical/Statistical numerical tool for the prediction of low Mach number, hydrodynamically-generated sound in the absence of cavitation. This tool is based on a mathematical formulation for the mean-shear (MS) component of the pressure in which RANS simulations provide the mean flow variables, while models based on turbulence simulations provide the necessary information regarding the fluctuating sources and their wall-normal correlations. Using turbulence simulations, all the elements of modeling can be tested since the exact three-dimensional source terms and their resultant wall pressures can be obtained. In the work reported herein we characterize the wall-pressure fluctuations due to the MS and TT pressures in both the convective and subconvective wavenumber-frequency ranges. This work is novel in three respects: (1) it characterizes the wavenumber-frequency characteristics of the individual MS and TT pressures, (2) it characterizes these pressures in the subconvective wavenumber-frequency range and (3) the MS and TT pressures have been decomposed into their components from four layers parallel to the wall. Thus, this work provides a first glimpse into the nature of the MS and TT pressures in a form appropriate for hydroacoustic modeling and it provides a database which can be used for validating models of the MS (and TT) pressures; in addition it shows the relationships between the the MS and TT velocity-field sources and their pressures in wavenumber-frequency space — this will help with physics-based modeling. The wall-pressure and velocity field databases were obtained from LES of a fully-developed, turbulent channel flow with  $Re_{\delta^*} = u_{\tau}\delta^*/\nu \approx 24$  ( $Re_{\tau} = 171$ ).

## ADMINISTRATIVE INFORMATION

This project was supported by the Office of Naval Research, contract number N0001499WX20508 (POCs: Candace Wark, L. Patrick Purtell). The NSWCCD Work Unit was 99-1-5200-059; Program Element 0601153N.

## ACKNOWLEDGEMENTS

The author would like to thank Dr. William K. Blake for providing motivation for this work and frequent guidance. Thanks are also due to Prof. Ugo Piomelli of the University of Maryland for providing the simulation code.

## INTRODUCTION

The US Navy is interested in turbulent wall pressure fluctuations (WPF) because they are an important source of energy for flow-induced noise. The low-wavenumber, high-frequency (with respect to the convective ridge) components (or subconvective) of WPFs provide the forcing function for the structures underlying the flow. The convective components provide the forcing function for flow-induced noise from trailing edge flows. The nature of the subconvective pressure has been difficult to determine, due to its low energy (with respect to the convective ridge), whereas the nature of the pressure at the convective ridge has been easier to determine due to its higher energy levels. Nonetheless, for modelling purposes, enough information from experiments has been hard to come by due to lack of three-dimensional data with which to characterize the velocity field wall pressure sources. Chang, Piomelli and Blake<sup>1</sup>, using a velocity field database from a low- $Re$  turbulent channel flow (TCF) decomposed the WPFs into their mean-shear (MS) and turbulence-turbulence (TT) components (partial pressures) and further, due to four regions of the channel (viscous shear layer, buffer layer, logarithmic region and upper channel). They showed in one-dimensional streamwise and spanwise wavenumber space which terms and regions are responsible for the dominant partial pressures. However, the one-dimensional spectra show essentially the character of the peak of the convective ridge, disguising the nature of the partial pressures away from the convective ridge, particularly in the subconvective wavenumber range. Chang, Piomelli and Blake<sup>1</sup> showed that the spectra of the individual TT pressures,  $\Pi_{ij}(Rr)$  (where  $Rr$  denotes one of the four regions of the channel) have two or more order of magnitude greater energy in the lowest wavenumber modes than the TT pressure due to all terms and regions. There is speculation that this high energy is due to low-wavenumber cross-channel coherence. Studying the  $k_x - \omega$  characteristics of the partial pressures may shed some more light on the nature of the low-wavenumber behavior.

In Chang<sup>2</sup> modelling the convective ridge pressure was addressed through the evaluation of a model for the MS pressure. A complete  $k_x - \omega$  spectrum of the MS pressure is necessary to guide model development, provide data for statistical functions and provide data for validation.

The objective of this work was to study the wavenumber-frequency characteristics of the partial pressures, particularly to assess the subconvective behavior and to study



computational issues that affect it. Two long time-series of partial pressures was obtained from a LES of a TCF simulation. From this database, the wavenumber-frequency spectra of the partial pressures was computed and evaluated.

## MATHEMATICAL FORMULATION

In this section we show the various forms for the nonlinear terms and suggest how they might impact computation of the wall pressure. The convection form, as derived from integral calculus, is given by

$$\mathbf{h} = \mathbf{u} \cdot \nabla \mathbf{u}, \quad (1)$$

the divergence form of  $\mathbf{h}$  is given by

$$\mathbf{h} = \nabla \cdot (\mathbf{u}\mathbf{u}), \quad (2)$$

the rotational form is given by

$$\mathbf{h} = \mathbf{u} \times \boldsymbol{\omega} + \frac{1}{2} \nabla (\mathbf{u} \cdot \mathbf{u}) \quad (3)$$

and the skew-symmetric form is given by

$$\mathbf{h} = \frac{1}{2} [\mathbf{u} \cdot (\nabla \mathbf{u}) + \nabla \cdot (\mathbf{u}\mathbf{u})]. \quad (4)$$

The form of the nonlinear terms,  $\mathbf{h}$ , in the Navier-Stokes equations may be important for the computation of the wall pressure directly and indirectly. The form of the nonlinear terms in the Poisson equation may have a direct affect on the wall pressure. The TT source terms are nonlinear velocity products derived directly from  $\mathbf{h}$ . The product of two sinusoidal signals are themselves signals that have wavenumbers which are the sum and difference of the two signal's respective wavenumbers. *e.g.*,

$$\sin \alpha \cos \beta = \frac{1}{2} \cos(\alpha - \beta) - \frac{1}{2} \cos(\alpha + \beta). \quad (5)$$

The nonlinear interactions result in the transfer of energy primarily into modes at the convective ridge. Energy is transferred to other parts of the spectrum, including the subconvective wavenumber range. The subconvective wavenumber range has energy levels that are at least 20 *dB* down from the convective ridge so it is conceivable that small changes in how  $\mathbf{h}$  are computed can affect the subconvective wavenumber range characteristics. For simplicity the divergence form has always been used for computing the nonlinear source terms.

The pressure is affected indirectly, in the computation of the velocity fields themselves in the N-S equations. When discretized, the convection form does not conserve linear momentum or kinetic energy; the divergence form conserves only linear momentum. This leads to numerical instabilities in turbulence simulations. However, it has been shown (see Zang<sup>3</sup>) that switching between the convective and divergence forms

(the “alternating” form) results in a well-behaved simulation. On the other hand, the rotation and skew-symmetric forms conserve both linear momentum and kinetic energy. It can be seen that the skew-symmetric form is the average of the divergence and convection forms, and thus closely related to the alternating form. The rotation form only requires the computation of six derivatives while the skew-symmetric form requires 18; the alternating form would take six and 12 derivative computations on alternating time steps. For efficiency reasons, the rotation form is the most popular, used for instance in Kim *et al.*,<sup>4</sup> and Choi and Moin<sup>5</sup>. Zang<sup>3</sup> showed that for a fully-developed turbulent channel flow the form of the nonlinear terms made differences in the high-wavenumber tail of the velocity spectra but did not affect the lower wavenumbers. However, in a simulation of homogenous turbulence it was shown that the rotation form significantly underpredicts the turbulence kinetic energy and velocity spectra. Also compared were the integral scales, microscales, skewness and flatness; it was found that the skew-symmetric and alternating forms had results much closer to the Galerkin method\* results than did the rotational results.

When the rotational form is used the resolved kinetic energy term is incorporated into the pressure term such that the computed pressure is  $P = p + \frac{1}{2}\mathbf{u} \cdot \mathbf{u}$ , where  $p$  is the dynamic pressure. Furthermore, the dynamic subgrid-scale model only computes the anisotropic part of the SGS stresses and the isotropic part is assumed to be added to the pressure term. For the present work the wall pressure is computed directly from the velocity fields. The nonlinear terms were evaluated with the rotational form for LES8 and the skew-symmetric form for LES9.

In both cases, the nonlinear terms were dealiased in the  $x$  and  $z$  directions using the 2/3 rule. In this method, the time advancement is performed on a “3/2-grid” in the  $x$  and  $z$  directions; the velocity fields are then converted to Fourier space where the top 1/3 modes in each direction are truncated, removing the aliasing errors from the velocities; the velocity fields are then transformed back into physical space. Restart files were written out on the 3/2 grid; these files were Fourier transformed, the top 1/3 modes were truncated (they are zero, anyway), inverse Fourier transformed and then written to file. For reading into the simulation, the velocity restart files were spectrally expanded onto the 3/2 grid.

Computation of the frequency spectra entails obtaining long time series of pressure data. The LES was run on a SGI Origin 200 (R10000 at 188 MHz). The CFL number was set to 0.14324 which corresponds to a time step  $\Delta t U_\ell / \delta = 0.025$ . This resulted in maximum Courant numbers of approximately 0.30, well below the stability limit of 0.50.

The LES8 database consists of 51 files with 64 realizations per file for a total of 3264 realizations spanning a time of  $326\delta/U_\ell$  ( $9.86\delta/u_\tau$ ). For each realization, 10 partial pressures were saved: four fields each of TT and MS pressure corresponding to the four regions and the TT and MS pressures from all regions.

---

\*In the Galerkin method the nonlinear terms are computed in wavespace rather than in physical space. This method is considered more accurate, but is much more computationally intensive.

The LES9 database consists of 20 files with 64 realizations per file for a total of 1280 realizations spanning a time of  $128\delta/U_\ell$  ( $9.86\delta/u_\tau$ ). For each realization, 11 partial pressures were saved: four fields each of TT and MS pressure corresponding to the four regions, the TT and MS pressures from all regions and the total pressure from all regions.

### Computation of partial pressures

Table 1. Regions of the channel.

Region	Limits	Description
1	$0 \leq y^+ < 5$	Viscous shear-layer
2	$5 \leq y^+ < 30$	Buffer layer
3	$30 \leq y^+ < 180$	Logarithmic region
4	$180 \leq y^+ < 360$	Upper channel

Since the wall-pressure depends on sources distributed throughout the entire flow domain it is difficult to ascertain where in the boundary layer the dominant sources are located. One advantage of turbulence simulations is that they generate three-dimensional velocity fields from which all the source terms can be computed. In this investigation the product of the sources by the Green's function, which is the true measure of the influence of the sources on the wall-pressure, has been computed. The channel was divided into four regions (Table 1) roughly corresponding to the viscous shear layer, buffer and logarithmic regions, and the upper part of the channel. The contribution of the source terms was integrated over each region. It is assumed that the partial pressures are evaluated at the lower channel wall, even though symmetry has been used in the data reduction and partial pressures have been averaged over both the upper and lower channel walls. The lower wall will be referred to as the "near-wall," the upper wall, the "far-wall."

The pressure source terms ( $T_{ij}$ ) were computed in physical space on the  $3/2$  grid. Nine terms were computed: the six TT terms, their sum, the MS term and the total. They were then Fourier-transformed to yield their complex coefficients in planar wavenumber space,  $\widehat{T}_{ij}(\mathbf{K}, y)$ . The integral of the product of the source terms and Green's function

$$\widehat{p}_{ij}(\mathbf{K}, Rr) = \int_{\eta_1(r)}^{\eta_2(r)} \widehat{T}_{ij}(\mathbf{K}, \eta) G(K, y = -1, \eta) d\eta. \quad (6)$$

(where  $\eta_1(r)$  and  $\eta_2(r)$  are the lower and upper integration limits for each region, and  $r$  denotes the vertical regions described in Table 1) was then computed using Chebychev integration. The complex partial pressure spectrum due to the source term  $T_{ij}$  from

region  $r$  is denoted by  $\hat{p}(\mathbf{K}, Rr)$ . The complex spectra for the various terms and regions could then be combined; *e.g.*, the partial pressure due to  $T_{12}$  from regions 2, 3 and 4 is

$$\hat{p}_{12}^{TT}(\mathbf{K}, R234) = \hat{p}_{12}^{TT}(\mathbf{K}, R2) + \hat{p}_{12}^{TT}(\mathbf{K}, R3) + \hat{p}_{12}^{TT}(\mathbf{K}, R4). \quad (7)$$

The total TT partial pressure is the summation of all the TT partial pressures,

$$\hat{p}^{TT}(\mathbf{K}, Rr) = \sum_{i=1}^3 \sum_{j=1}^3 \hat{p}_{ij}^{TT}(\mathbf{K}, Rr), \quad (8)$$

and the total partial pressure is

$$\hat{p}^{tot}(\mathbf{K}, Rr) = \hat{p}^{MS}(\mathbf{K}, Rr) + \hat{p}^{TT}(\mathbf{K}, Rr). \quad (9)$$

The total pressure is  $\hat{p}^{tot}(\mathbf{K}, R1234)$ .

The magnitudes of the complex spectra were computed by

$$\Pi(\mathbf{K}, Rr) = \hat{p}_{ij}^*(\mathbf{K}, Rr) \hat{p}_{ij}(\mathbf{K}, Rr) \quad (\text{no summation}) \quad (10)$$

(where  $\hat{f}^*$  is the complex conjugate of  $\hat{f}$ ), and averaged over multiple realizations. It should be noted that the partial pressures are defined by the integral over all frequencies,

$$\Pi(\mathbf{K}, Rr) = \int_{-\infty}^{\infty} \Pi(\mathbf{K}, \omega, Rr) d\omega \quad (11)$$

where  $\Pi(\mathbf{K}, \omega, Rr)$  is the partial pressure in four-space. The one-dimensional spectra were obtained by the integrations

$$\pi(k_x, Rr) = \int_{-\infty}^{\infty} \Pi(\mathbf{K}, Rr) dk_z \quad (12)$$

and

$$\pi(k_z, Rr) = \int_{-\infty}^{\infty} \Pi(\mathbf{K}, Rr) dk_x \quad (13)$$

The one-dimensional spectra were normalized by  $\tau_w^2 \delta$ .

### Computation of partial pressure spectra

The wavevector-frequency spectra shown in this Section were computed by the following methodology: the data were divided into  $N_t = 384$  point segments spanning the period,  $T$ , with 50 percent overlap. This gave a reasonable compromise between number of spectra realizations and frequency resolution (the frequency resolution is approximately  $4u_\tau/\delta$  and the  $0.1\delta/u_\tau$  sampling rate gives a maximum frequency of approximately  $760u_\tau/\delta$ ). A Hanning window was used on the time segments, while no windowing was necessary in the  $x$  and  $z$  directions in which the flow is periodic. The Hanning window was applied in time to the total, resolved pressure,  $\bar{p}$ , normalized by the long time average value of  $\tau_w$ ,

$$\tilde{p}(x_i, z_j, t_l) = \bar{p}(x_i, z_j, t_l) \frac{1}{2} \left( 1 - \cos \frac{2\pi l}{N_t} \right) \quad (14)$$

where  $i = 1 \dots N_x$ ,  $j = 1 \dots N_z$ , and  $l = 1 \dots N_t$ . A three-dimensional Fourier wavenumber-frequency transform of each time segment was taken and from that, an averaged spectral density was obtained from the mean of the spectral densities from the  $m$  overlapping segments

$$\Psi(i\Delta k_x, j\Delta k_z, l\Delta\omega) = \frac{1}{m} \sum_{s=1}^m (\hat{p} \hat{p}^*)_s. \quad (15)$$

Here  $\hat{p}$  denote the Fourier coefficients of the pressure and  $\hat{p}^*$  are their complex conjugates. The three-dimensional spectral density should satisfy Parseval's theorem which states that the "mean square value of a periodic function is equal to the sum of squares of all it Fourier coefficients,"<sup>6</sup>

$$\frac{1}{N_x N_z N_t} \sum_{l=1}^{N_t} \sum_{j=1}^{N_z} \sum_{i=1}^{N_x} p^2(x_i, z_j, t_l) = \sum_{l=1}^{N_t} \sum_{j=1}^{N_z} \sum_{i=1}^{N_x} \Psi(i\Delta k_x, j\Delta k_z, l\Delta\omega) \quad (16)$$

where the left hand side is the mean-square (MS) pressure. Since the pressure has been windowed in time, its spectral density does not satisfy (16) exactly;  $\Psi$  is then normalized to satisfy (16). The two-dimensional  $k_x - \omega$  spectra is given by the summation over all the spanwise wavenumber modes,

$$\Phi(i\Delta k_x, l\Delta\omega) = \sum_{j=1}^{N_z} \Psi. \quad (17)$$

The two-dimensional spectral density extends over  $l = 1 \dots N_t$  frequency bins and  $i = 1 \dots N_x$  wavenumber bins and has the symmetry property

$$\Phi(i\Delta k_x, l\Delta\omega) = \Phi[(N_x - i + 2)\Delta k_x, (N_t - l + 2)\Delta\omega] \quad (18)$$

In the  $k_x - \omega$  plots the wavenumber bins  $N_x/2 + 2 \leq i \leq N_x$  have been translated to the bins  $-N_x/2 + 1 \leq i \leq -1$ ; with this convention, a wave that is convecting downstream will have either  $\omega$  or  $k_x$  negative. In the two-dimensional spectra plots, the convective ridge, representing energy convecting downstream, is shown in the negative  $k_x$ , positive  $\omega$  quadrant. Constant frequency cuts of streamwise wavenumber spectra, extracted from this two-dimensional spectra, show just the negative  $k_x$ , *i.e.*, where the convective ridge lies.

The one-dimensional point frequency spectra is obtained from the double summation

$$\phi(l\Delta\omega) = \sum_{j=1}^{N_z} \sum_{i=1}^{N_x} \Psi(i\Delta k_x, j\Delta k_z, l\Delta\omega), \quad (19)$$

and the one-dimensional wavenumber spectra are given by

$$\phi(i\Delta k_x) = \sum_{j=1}^{N_z} \sum_{l=1}^{N_t} \Psi(i\Delta k_x, j\Delta k_z, l\Delta\omega), \quad (20)$$

and

$$\phi(j\Delta k_z) = \sum_{i=1}^{N_x} \sum_{l=1}^{N_t} \Psi(i\Delta k_x, j\Delta k_z, l\Delta\omega). \quad (21)$$

These are functions which are symmetric about their folding frequency (or wavenumber); they have been converted to one-sided spectra by multiplying all components, except the zero frequency (or wavenumber) component, by a factor of 2, thus preserving Parseval's identity.

Note that two normalizations have been used in our previous works:

1. The wall-pressure spectra shown in Chang *et al.*<sup>7</sup> and Chang<sup>2</sup> are derived from three-dimensional  $k_x - k_z - \omega$  spectra. In these works, three-dimensional spectra was normalized using a Parseval's equation in which the *integral* of the spectra equalled the m.s. of the input signal. The various summations *e.g.*, (19)-(21) were normalized such that their *integrals* are equal to the m.s.. The rationale for this approach was for dimensional consistency: it is assumed that the three-dimensional spectra has the units of  $p^2 L^2 T$ ; integrating over  $k_z$  (summing all  $k_z$  components and multiplying by  $\Delta k_z$ ) gives the units  $p^2 L T$ ; subsequent integration over  $k_x$  to obtain the point frequency spectrum gives the units  $p^2 T$  which is typically found in the literature (see *e.g.*, Keith *et al.*<sup>8</sup>).
2. The second normalization, used in the present work, as well as for the partial pressure spectra in Chang<sup>2</sup> is based on the principle that the *summation* of the spectra equals the m.s.. In this case there is no explicit way to change the units when performing the various integrations. It will be assumed that the units of the  $k_x - k_z - \omega$  spectra are  $p^2 L^2 T$ ; the  $k_x - k_z$  spectra  $p^2 L^2$ ;  $k_x - \omega$  and  $k_z - \omega$  spectra  $p^2 L T$ ; one-dimensional  $k_x$  and  $k_z$  spectra  $p^2 L$ ; and one-dimensional  $\omega$  spectra  $p^2 T$ .

To convert from the first to second normalization, simply multiply the streamwise wavenumber spectra by  $\Delta k_x$ , the spanwise wavenumber spectra by  $\Delta k_x$  and the frequency spectra by  $\Delta\omega$ .

## PRESENTATION OF RESULTS

### Mean velocity and turbulence intensity profiles

In this subsection we show the statistics of the partial pressures. The mean velocity profiles are shown in Figure 1. Comparison to DNS results show that they are well-resolved and have the expected behavior in the various regions of the channel. Turbulence intensity profiles are shown in Figure 2.

### Mean square variation of pressure with time

Figure 3 shows the variation of the TT, MS and total pressures due to sources over the entire channel[R(1234)]. The m.s. pressures have been normalized by  $(\rho u_\tau^2 \delta)^2$ ,

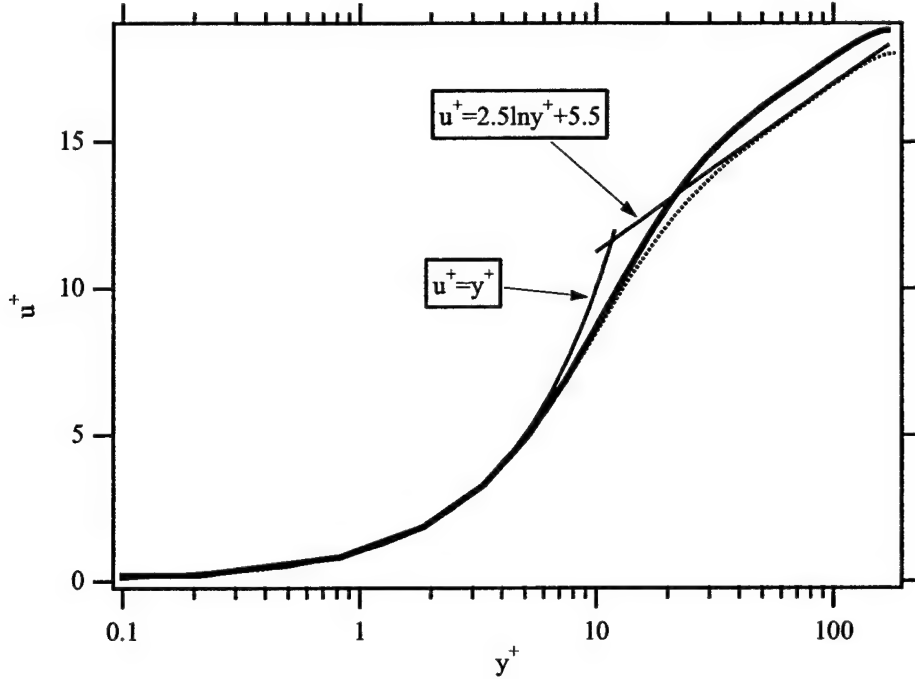


Figure 1. Viscous-scaled mean velocity profiles; — : LES8; ..... : DNS5.

while time has been normalized by  $\delta/U_\ell$ . It shows clearly that the MS pressure is almost always greater than the TT pressure and that the largest variations in the total pressure are highly correlated with those variations in the MS pressure. By contrast, the TT pressure has a much smaller variation than either the MS or total pressure (even though it can be seen that the TT variation are correlated with the MS and total pressure). This result is an indication that, at least in a broad-band sense, and over the entire domain, high amplitude events are more closely associated with the MS pressure than the TT pressure. This is consistent with the findings of Johansson *et al.*<sup>10</sup>.

### Point frequency spectra

The objective of this subsection is to show that the LES8 compares very well with previous simulations and recent experiments.

Figure 4 compares the point frequency spectra for LES8, DNS5, and the TBL simulation of Singer<sup>11</sup>. Also shown are two recent experimental results by Farabee and Casarella<sup>12</sup> and Gravante *et al.*<sup>13</sup> with  $Re_\tau$  values similar to that of Singer. The important parameters for the point frequency spectra are listed in Table 2. Figure 4(a), the spectra normalized by outer variables, shows that for the low frequencies, the LES and DNS spectra are identical. For  $\omega\delta/u_\tau > 100$  the LES and DNS spectra diverge rapidly, due to the simulations respective wavenumber resolutions — the point frequency spectra is the integration over all wavenumbers, and it can be seen in Figure 4, that as the frequency increases, the amount of energy truncated by the wavenumber cutoff increases. In fact, at about  $\omega\delta/u_\tau = 140$ , only about one-half the convective ridge is resolved and the difference between the LES and DNS is about 3 dB.

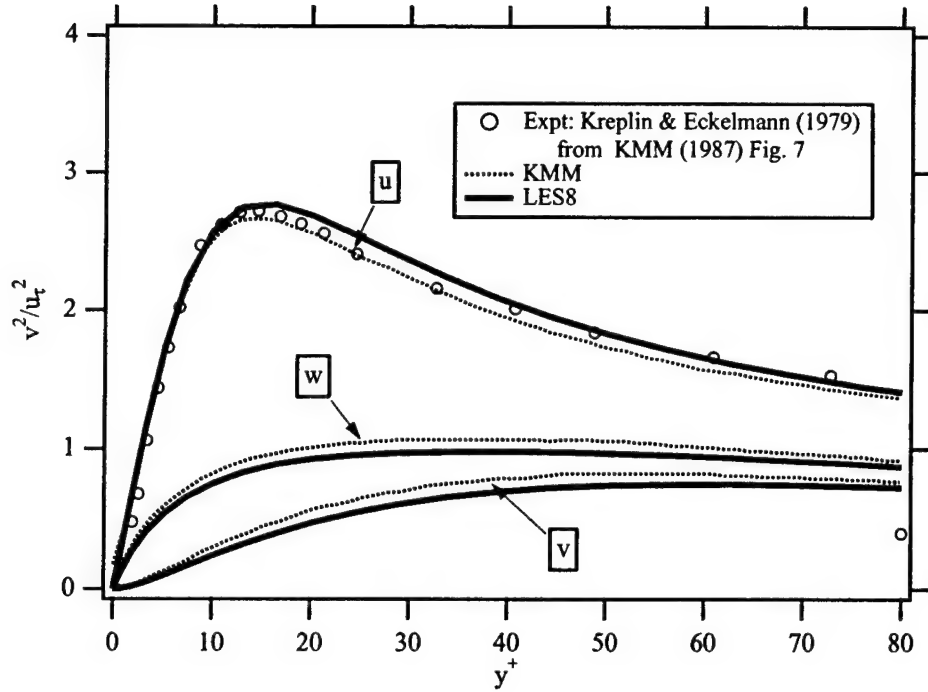


Figure 2. Turbulence intensity profiles; — : LES8; ..... : Kim *et al.*<sup>4</sup>;  $\circ$  : Kreplin and Eckelmann<sup>9</sup>

The simulation of Singer has lower energy than LES8 and DNS5 in the lower frequencies, but is virtually identical with that of Gravante *et al.*<sup>13</sup>. The data of Farabee and Casarella<sup>12</sup> is slightly lower. This variation in the low frequencies is consistent with the trends shown in Keith *et al.*,<sup>8</sup> who compared point frequency spectra over a wide range of  $Re$ . Farabee and Casarella<sup>12</sup>, on the other hand, showed that with a two-fold variation in  $Re$ , this frequency range, that includes the peak of the spectra, should collapse to a single curve.

It is apparent that the higher  $Re$  spectra has a much larger spectra peak region than does the lower  $Re$  LES8 and DNS5 data. This is consistent with the notion that higher  $Re$  flows have more energy in the scales small compared with  $\delta$ . The overlap range, as proposed by Bradshaw<sup>14</sup> should have a  $\omega^{-1}$  decay rate. The spectra of Gravante *et al.*<sup>13</sup> is the only one that exhibits an extended frequency range with such behavior. The TCF data has no such region, since low  $Re$  flows have essentially no wavenumber separation between the larger, energy producing scales and the smaller energy dissipating scales. The data of Singer may have a small frequency range that has a  $\omega^{-1}$  decay rate; however, it too, is attenuated rapidly by the simulation's wavenumber resolution. The data of Farabee and Casarella<sup>12</sup> has an approximate  $\omega^{-1/2}$  decay rate, but no  $\omega^{-1}$  region.

The inner-scaled spectra, Figure 4(b), shows that inner scaling does a fairly good job of collapsing all of the spectra, with differences explainable by wavenumber resolution arguments (values of  $\omega_c^+$ , the frequencies where one-half of the convective ridge is resolved, are listed in Table 2). In the range  $\omega^+ < 1$  ( $\omega^+ \equiv \omega\delta^+/u_\tau$ ) the TCF data



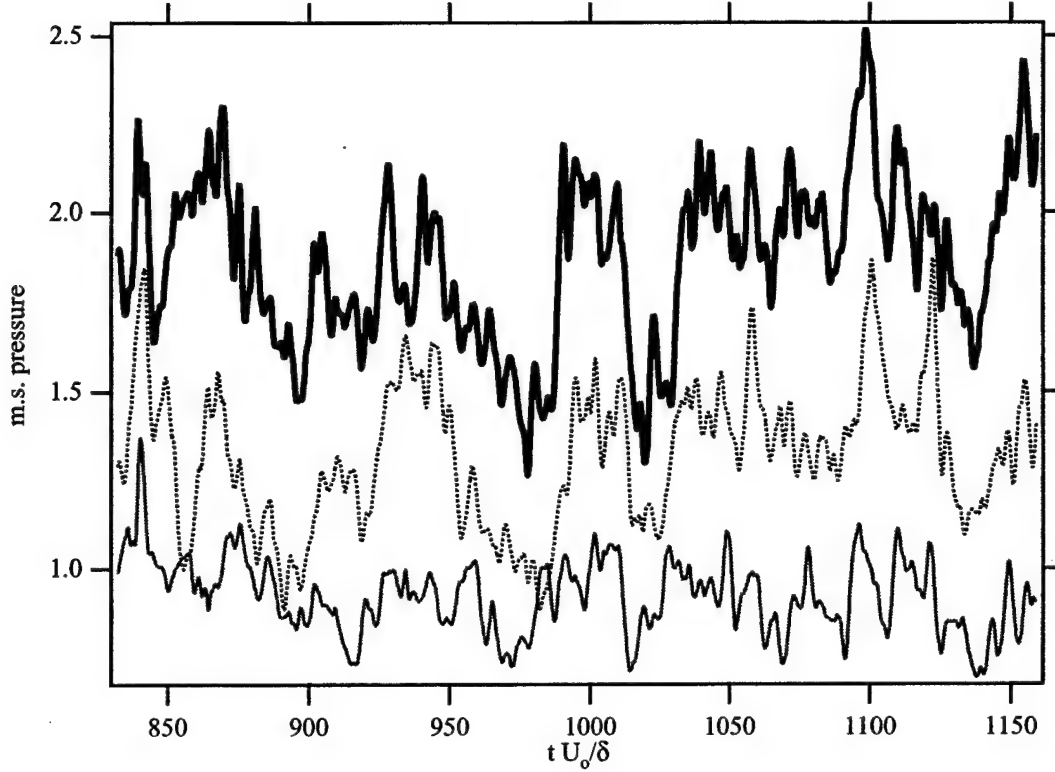


Figure 3. Temporal variation of m.s. (mean-square) TT, MS and total pressures (R1234); — : TT, ..... : MS, and — : total.

and Gravante *et al.*<sup>13</sup> are identical. Both the DNS and Gravante *et al.*<sup>13</sup> have a range with a  $\omega^{-5}$  decay rate; the DNS data diverges at about  $\omega^+ > 2$  due to wavenumber resolution, whereas the data of Gravante *et al.*<sup>13</sup>, has a  $\omega^{-5}$  behavior out to its largest frequency; this is because it has  $\omega_c^+ = 5$ . As expected, the spectra of Singer decays most rapidly due to wavenumber resolution: due to the coarse grid ( $d^+ = 100$ ) Singer's data has  $\omega_c^+ = 0.4$ ; the LES8 data has  $\omega_c^+ = 0.8$ . The data of Farabee and Casarella<sup>12</sup> is slightly lower than the data of Gravante *et al.*<sup>13</sup> and has a frequency range with a constant decay rate slightly larger than  $\omega^{-5}$ . The reason for the faster decay rate is that it has  $\omega_c^+ > 0.8$ . Above  $\omega_c^+ > 0.8$  the spectra of Farabee and Casarella<sup>12</sup> does not decay as fast as the simulations.

Table 2. Wall pressure frequency spectra parameters.  $Re_o \equiv U_o \delta / \nu$ , where  $U_o$  is the channel centerline velocity for channel flow and free stream velocity for boundary layer flows.

Source	$Re_o$	$Re_\tau$	$d^+$	$\omega_c^+$
LES8	3200	171	44	0.8
DNS5	3200	180	18	2.1
Singer	25,500	1000	100	0.4
Farabee and Casarella <sup>12</sup>	39,000	1535	44	0.8
Gravante <i>et al.</i> <sup>13</sup>	40,000	1504	8	5

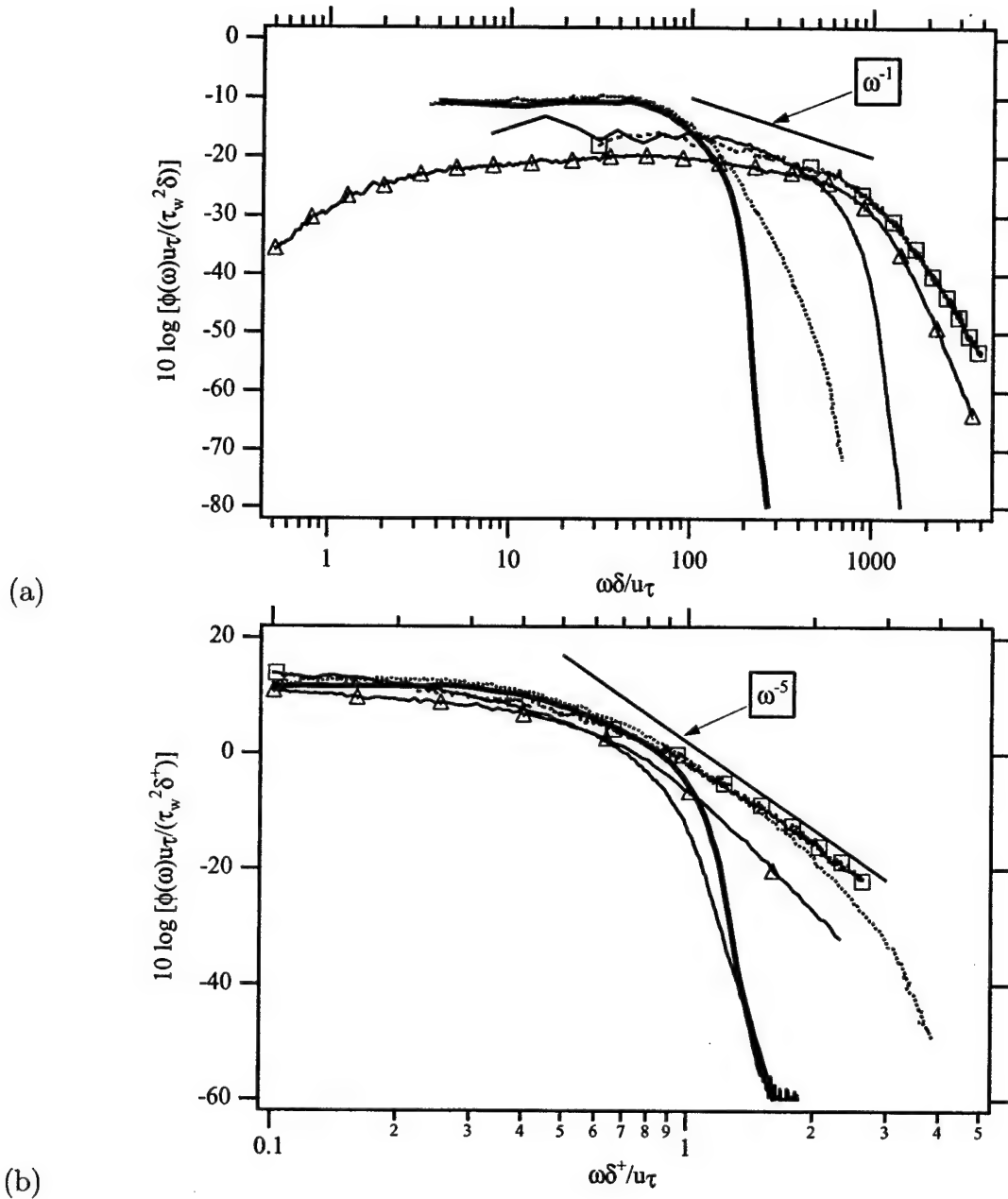


Figure 4. Comparison of (a) outer- and (b) inner-scaled ( $\delta^+ \equiv \nu/u_\tau$ ) point frequency spectra; — : LES8, ..... : DNS5, — : Singer.<sup>11</sup>  $\Delta$  : Farabee and Casarella<sup>12</sup>, and  $\square$  : Gravante *et al.*<sup>13</sup>.

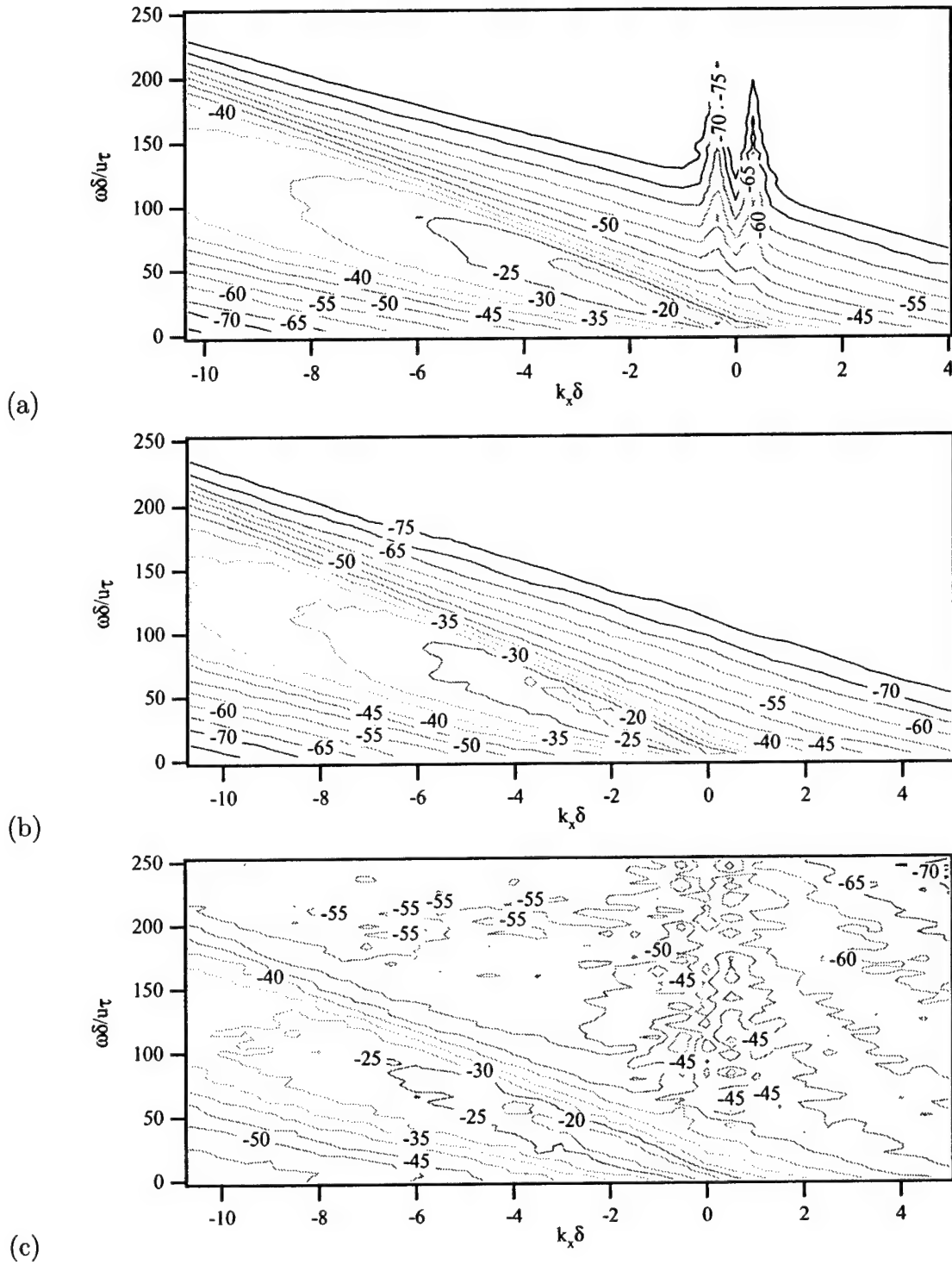


Figure 5. Two-dimensional contour plots of  $k_x - \omega$  spectra for  $\pi^{Tot}(R1234)$ ; (a) LES8 (rotational) (b) LES9 (skew-symmetric) (c) Choi and Moin.<sup>5</sup>

### $k_x - \omega$ spectra— R1234

In this subsection we show the two-dimensional  $k_x - \omega$  spectra for the total pressure from all regions and compare it to that from the literature and previous simulations. Figure 5 shows the two-dimensional spectra from LES8, LES9 and from Choi and Moin.<sup>5</sup> (reduced by Bruce Abraham and shown in Chang, Abraham and Piomelli<sup>7</sup>). The CM data have not been adjusted for the change in normalization and only the wavenumber-frequency range corresponding to LES8 is shown. The character of the subconvective range is quite different: the data of CM has much higher energy, basically flattening out, as has been noted previously. The LES8 data falls off rapidly with decreasing  $|k_x|$  with the energy build-up in the the smallest  $|k_x|$  modes; the LES9 data is flat in the smallest  $|k_x|$  modes.

Figure 6 are constant- $\omega$  cuts comparing LES8, LES9 and CM. The CM data has a convective ridge that is both higher and wider than the LES; this is consistent with previous findings. What is notable is that in the subconvective range the CM data tends toward a  $k_x^0$  behavior as  $\omega$  increases, whereas the LES8 and LES9 data has an increasingly large rolloff in this range. The LES9 data is quite different than the LES8 data in the lowest  $|k_x|$  modes: it is flat, not having the energy build-up as in LES8.

### Partial MS and TT pressures — R1234

Figure 7 shows the one-dimensional spectra of total, MS and TT pressures due to sources over the entire channel. The streamwise and spanwise spectra are similar to the DNS data shown in Chang, Piomelli and Blake<sup>1</sup>. The plots show that the low wavenumbers and frequencies are dominated by the MS pressure; in the spanwise wavenumber and frequency mid-range both TT and MS contribute significantly to the total pressure; at high spanwise wavenumbers the TT pressure becomes dominant (see *e.g.*, the spanwise spectra, Figure 7(b)).

Plots of the two-dimensional  $k_x - \omega$  spectra of the total, MS and TT partial pressures due to sources from the entire channel (R1234) for LES8 and LES9 are shown in Figures 8 and 9, respectively. Figure 8(a) shows that the total pressure has an energy buildup in the lowest wavenumbers. Comparison with Figures 8(b) and (c) shows that this buildup must come from the TT pressure; the MS pressure falls off rapidly in the lowest  $|k_x|$  bins. Both the TT and total pressure for LES9, Figure 9, have smooth contours with no buildup in the lowest  $|k_x|$  bins. The MS pressure for LES9 is identical to that shown for LES8 in Figure 8(b).

Greater insights into the nature of the subconvective wavenumber range can be obtained from constant frequency plots of streamwise wavenumber spectra, Figure 10 (LES8) and Figure 11 (LES9). It is obvious that the TT pressure is the source of the subconvective pressure as the MS pressure goes to zero as  $k_x \rightarrow 0$ . At the lower frequencies, Figure 10(a) and Figure 11(a), the subconvective range is flat; as frequency increases [Figures 10(b)-(d) (LES8) and Figures 11(b)-(d) (LES9)], the energy increases as  $k_x \rightarrow 0$ . At the lower frequencies the MS and TT contributions at the convective ridge are about equal. As frequency increases, the MS becomes the dominant pressure at the convective ridge. Though the wavenumber resolution limits our ability to make a

conclusive statement, it appears that the high wavenumber side of the convective ridge is dominated by the MS pressure.

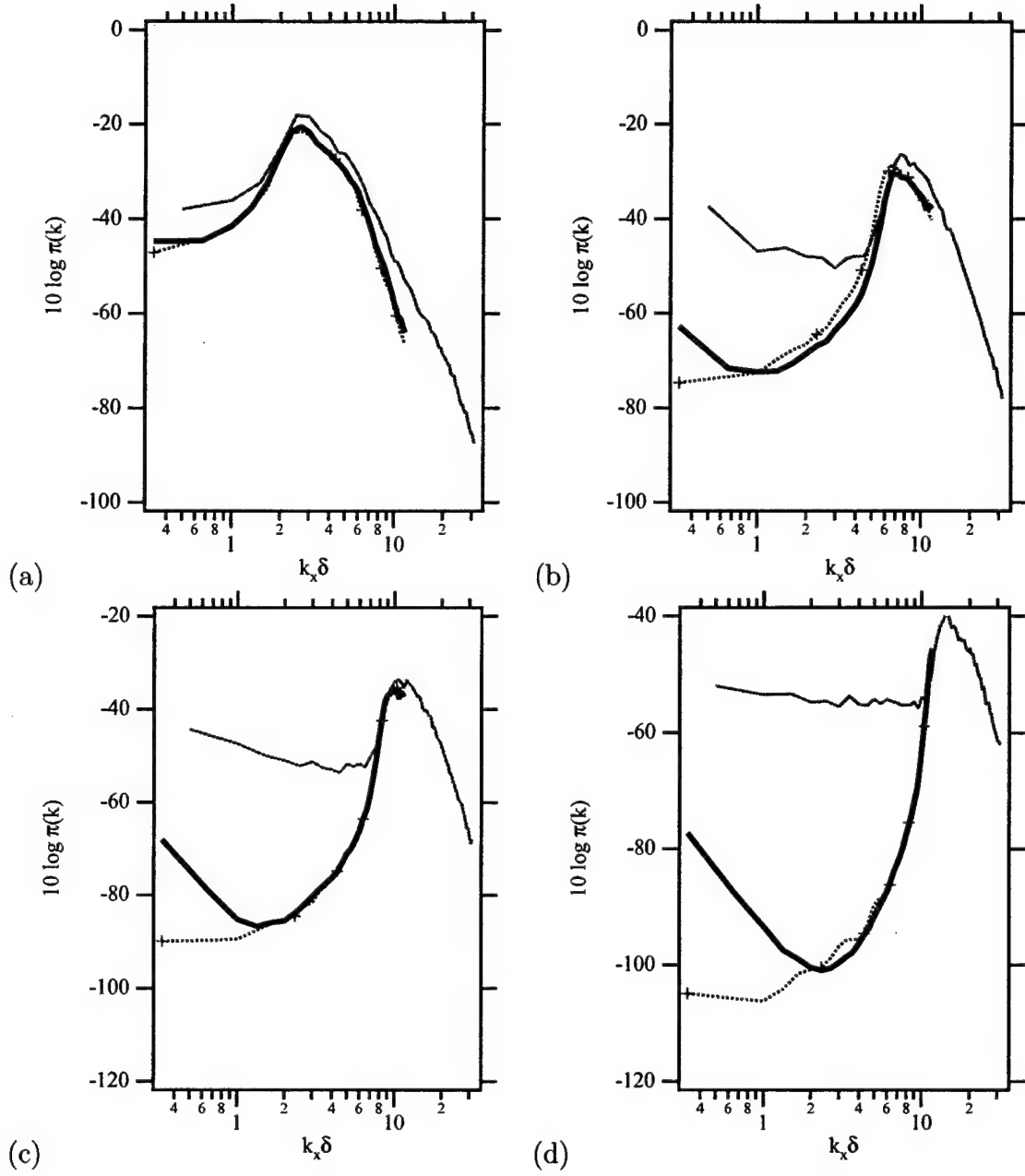


Figure 6. Constant frequency cuts of  $k_x - \omega$  spectra of total pressures from entire channel (R1234); (a)  $\omega\delta/u_\tau = 44$  (b)  $\omega\delta/u_\tau = 108$  (c)  $\omega\delta/u_\tau = 156$  and (d)  $\omega\delta/u_\tau = 204$ ; — : LES8; + : LES9; — : CM.

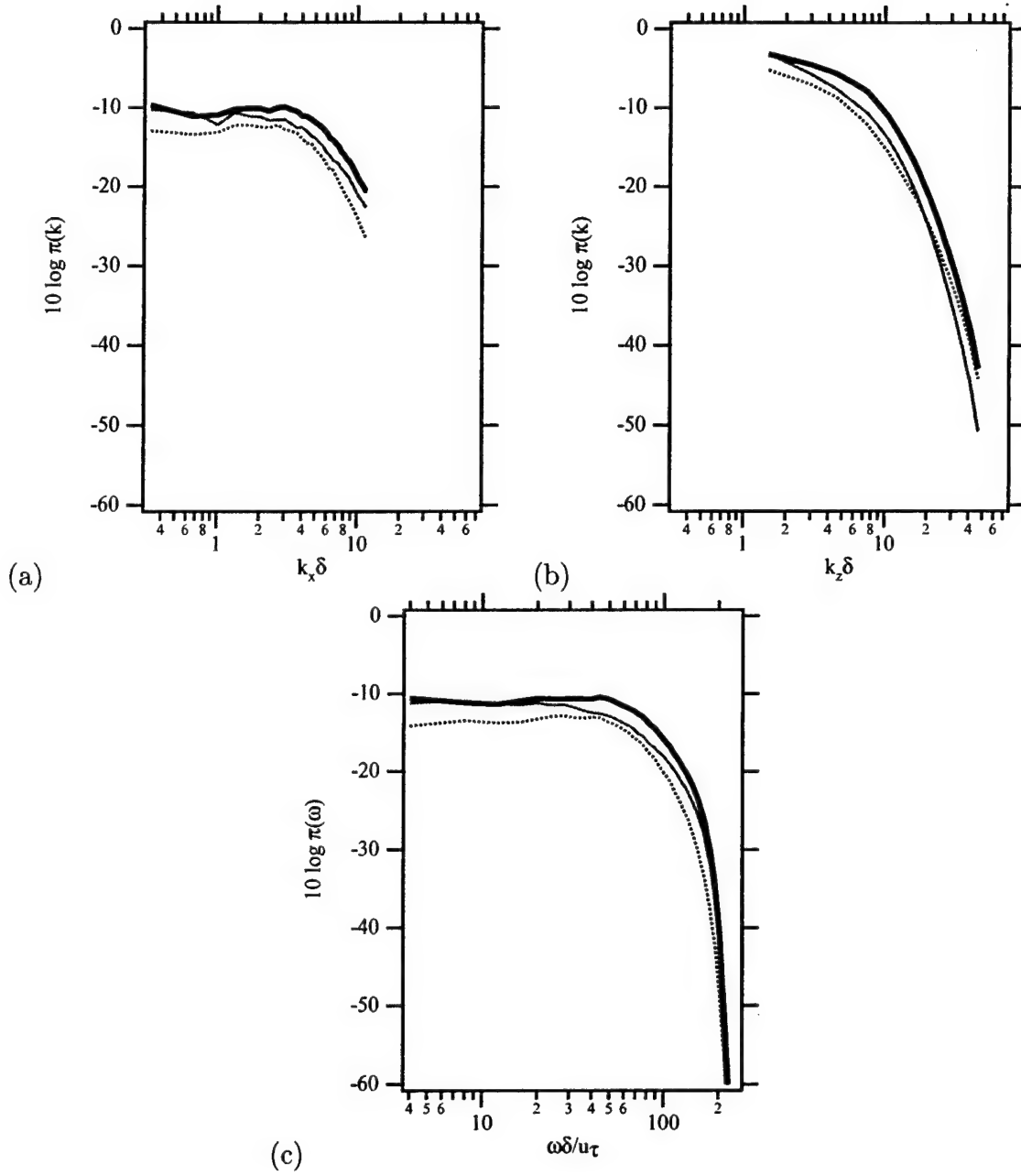


Figure 7. One-dimensional spectra of partial pressures for sources integrated over entire channel (R1234). — :  $\pi^{tot}$ ; — :  $\pi^{MS}$ ; ..... :  $\pi^{TT}$ ; (a) streamwise wavenumber (b) spanwise wavenumber and (c) frequency.



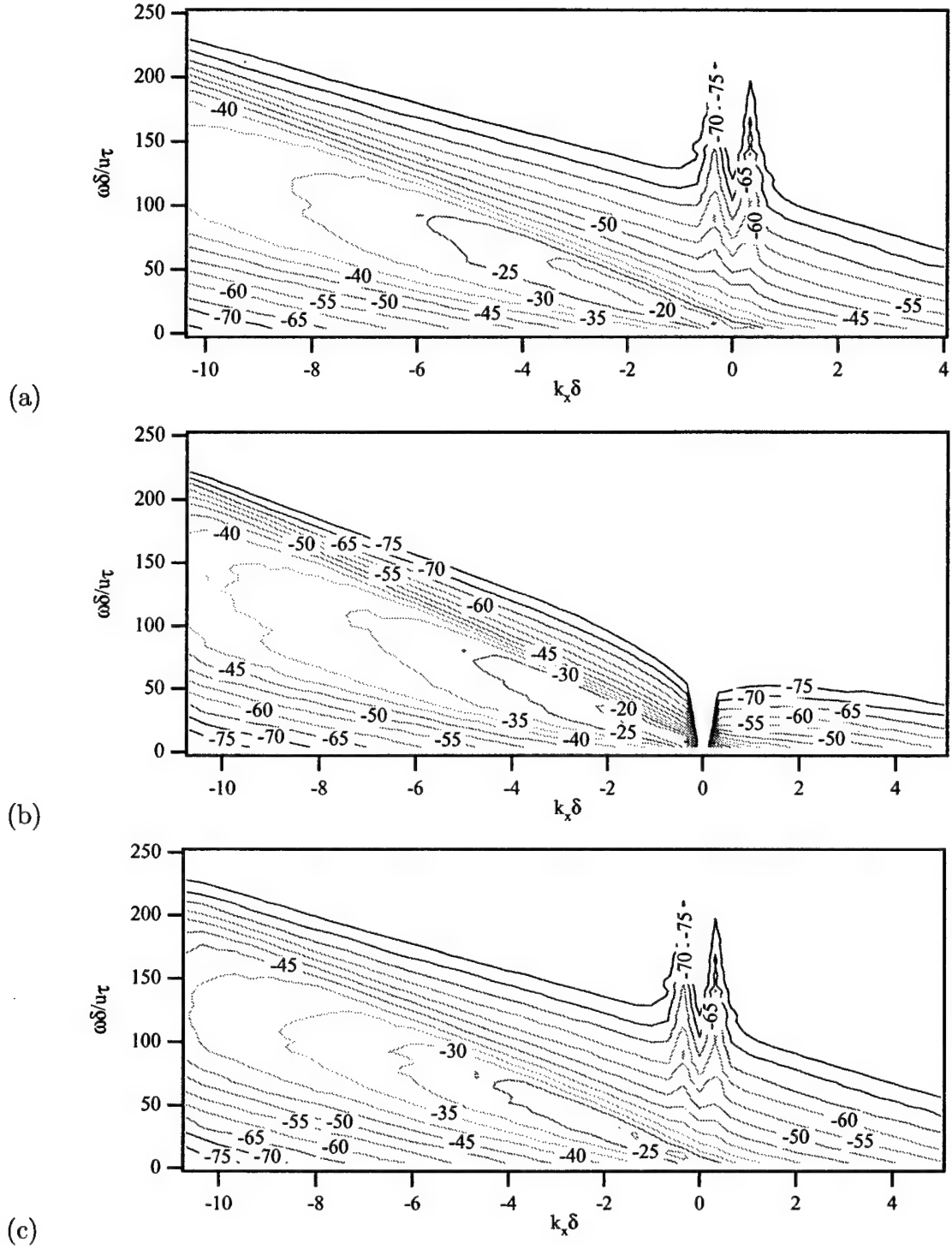


Figure 8. Two-dimensional contour plots of  $k_x - \omega$  spectra from LES8 for all regions (R1234); (a)  $\pi^{Tot}$  (b)  $\pi^{MS}$  and (c)  $\pi^{TT}$ .

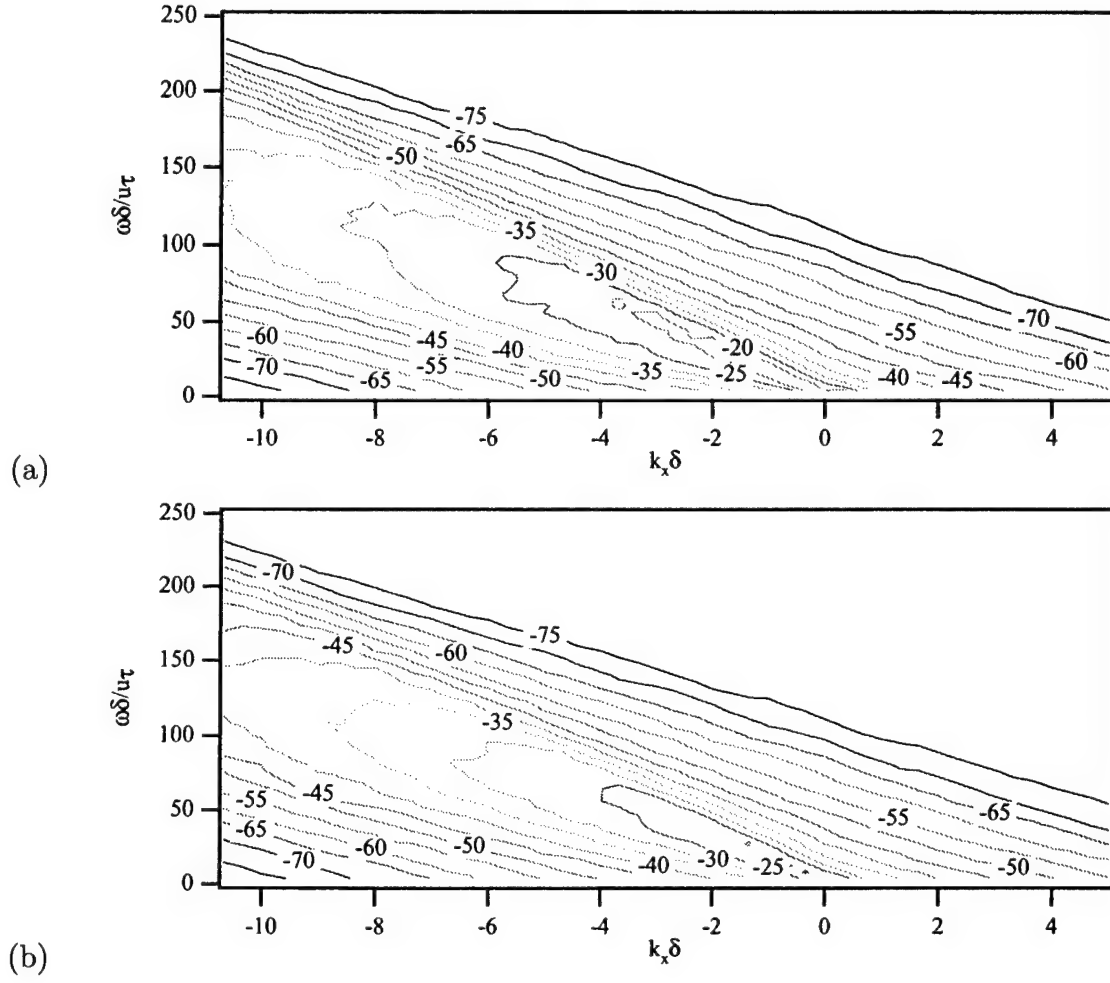


Figure 9. Two-dimensional contour plots of  $k_x - \omega$  spectra from LES9 for all regions (R1234); (a)  $\pi^{Tot}$  and (b)  $\pi^{TT}$ .

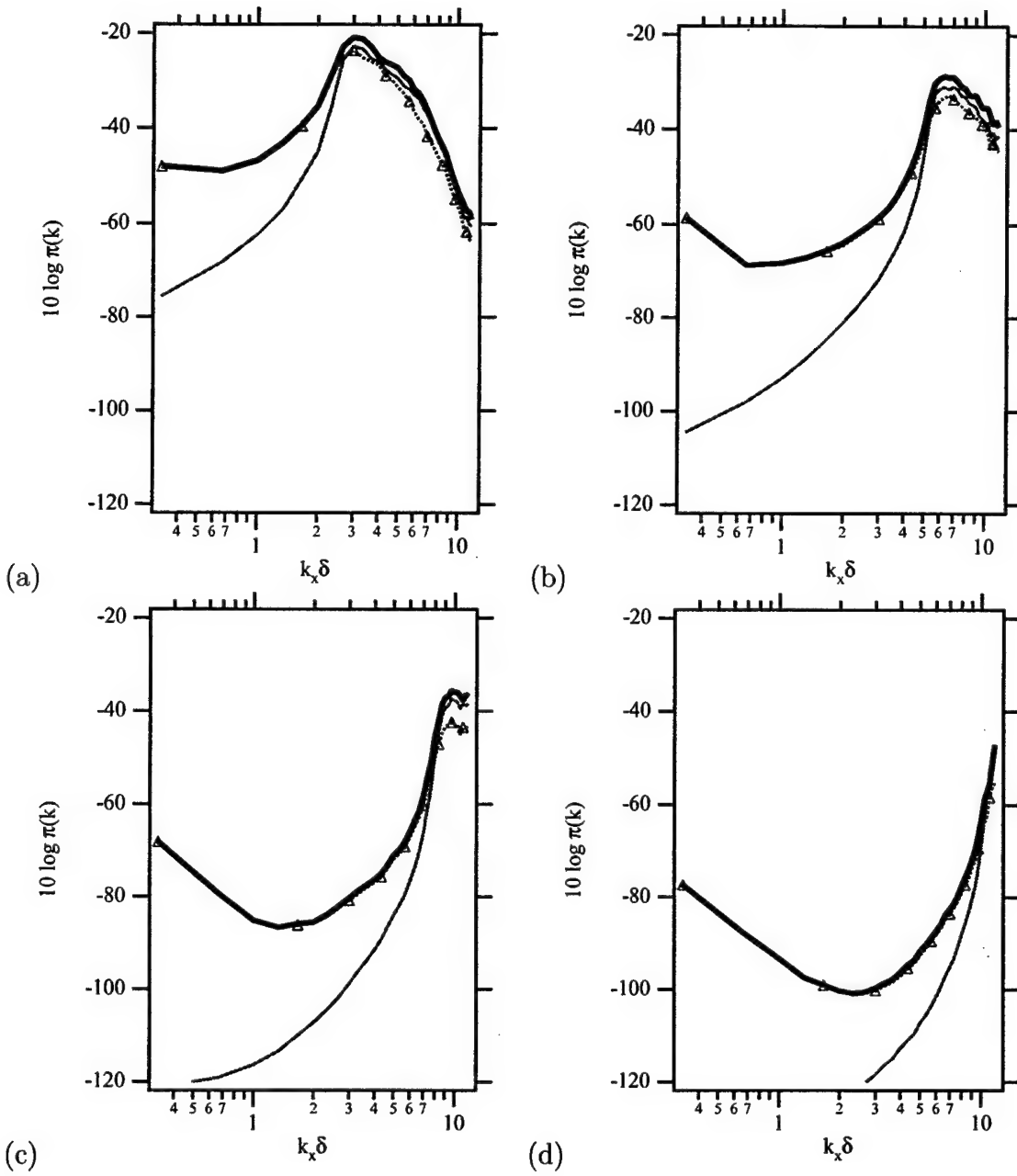


Figure 10. Constant frequency cuts of  $k_x - \omega$  spectra of partial pressures from LES8 for all regions (R1234); (a)  $\omega\delta/u_\tau = 52$  (b)  $\omega\delta/u_\tau = 104$  (c)  $\omega\delta/u_\tau = 156$  and (d)  $\omega\delta/u_\tau = 204$ ; — : total; — : MS;  $\triangle$  : TT.

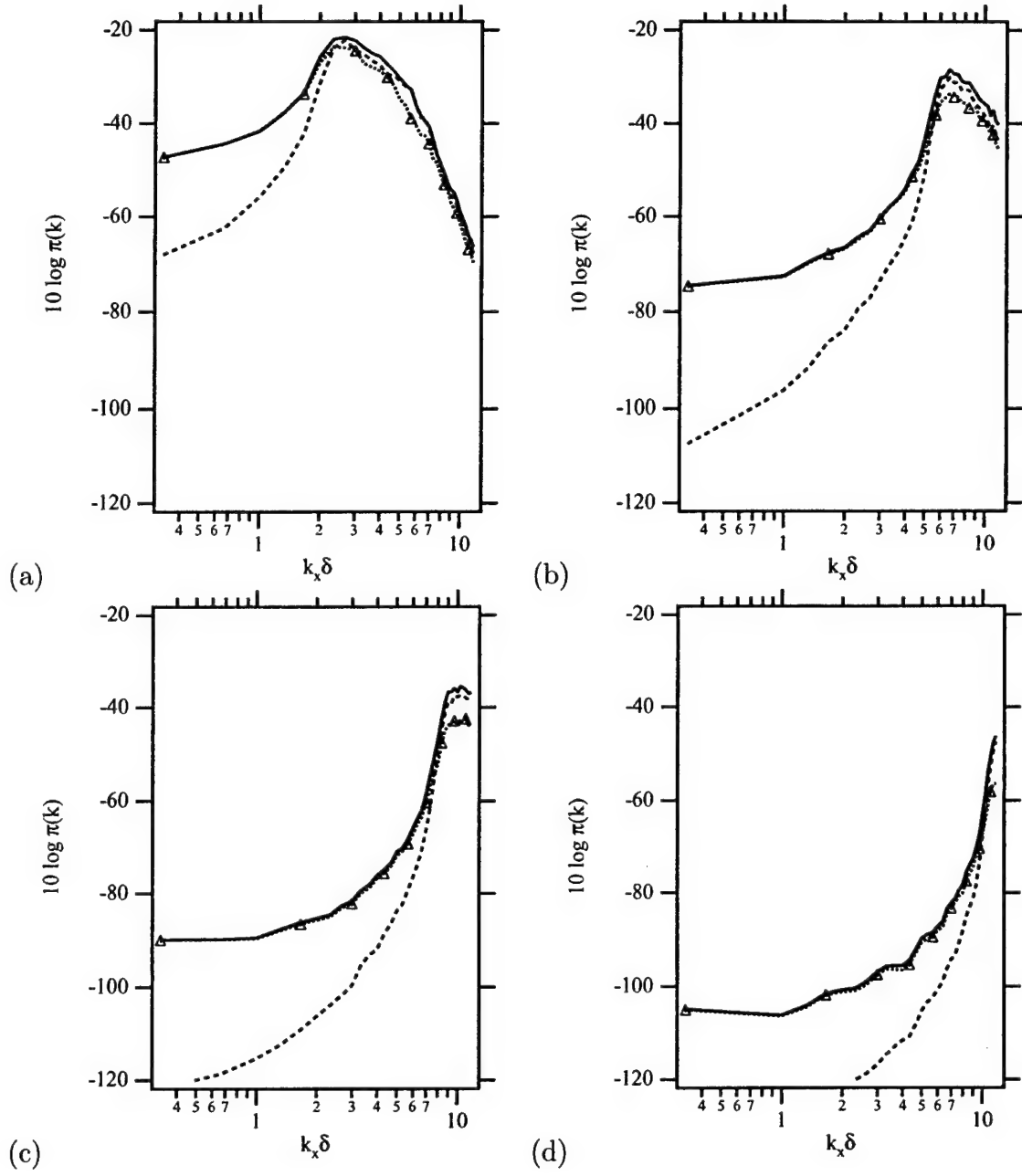


Figure 11. Constant frequency cuts of  $k_x - \omega$  spectra of partial pressures from LES9 for all regions (R1234); (a)  $\omega\delta/u_\tau = 44$  (b)  $\omega\delta/u_\tau = 108$  (c)  $\omega\delta/u_\tau = 156$  and (d)  $\omega\delta/u_\tau = 204$ ; — : total; ..... : MS;  $\triangle$  : TT.

## Partial pressures from regions of channel

In this subsection we look at the partial pressures from four regions of the channel.

### One-dimensional spectra of partial pressures

Figure 12 shows the one-dimensional MS pressure spectra for all regions of the channel and for each of the individual regions. The streamwise and spanwise spectra are similar to the DNS5 data shown in Chang, Piomelli and Blake<sup>1</sup>. The frequency spectra have previously not been shown. The figures show that the buffer layer dominates the entire wavenumber and frequency ranges; the logarithmic region is the next most dominant; the viscous shear layer is small at low  $k_x - \omega$ , increasing with  $k_x - \omega$ ; all regions except the viscous shear layer are important at low  $k_x - \omega$ .

The one-dimensional TT pressure spectra for all regions of the channel and for each of the individual regions from LES8 are shown in Figure 13. The plots for LES9 are virtually identical and have not been included. It shows the familiar low  $k_x - \omega$  energy buildup shown in Chang, Piomelli and Blake<sup>1</sup>. The low-frequency energy buildup indicates that the partial pressures have high-energy slowly-varying components. These have been observed in animations of the TT partial pressures.

### Two-dimensional $k_x - \omega$ spectra of partial pressures

Figures 14 and 15 show the MS spectra for sources from each of the regions, respectively. It is apparent that with increasing distance from the wall, the slope of the convective ridge in  $k_x - \omega$  space ( $\omega/(k_x\delta)$ ) increases; the width of the convective ridge decreases; the shape of the convective ridge becomes increasingly asymmetric; the energy in the higher wavenumbers and frequencies becomes attenuated, becoming increasingly concentrated in low  $k_x - \omega$ . The TT  $k_x - \omega$  spectra from the four regions are shown in Figures 16 and 17 for LES8 and Figures 18 and 19 for LES9. The figures show that both LES8 and LES9 have similar energy build-ups in the low-wavenumbers. However, as shown previously, when the pressures from all the regions are added together LES8 and LES9 are quite different: Figure 8(a) and (c) shows that for LES8 the TT partial pressure (and total, too) from all regions retains the low- $|k_x|$  energy buildup. On the other hand, Figure 9(a) and (b) show that adding the contributions from all regions results in the low- $|k_x|$  energy buildup disappearing.

### Convection velocities

As noted above, the convection velocities computed from the peak of the convective ridge can characterize the  $k_x - \omega$  behavior of the peak. These were computed from

$$U_c(k_x) = \frac{\omega_{peak}(k_x)}{k_x u_\tau} \quad (22)$$

and are shown in Figure 20 for the MS and TT partial pressures from each of the regions.  $U_c$  increases with distance from the wall, from about  $10u_\tau$  due to viscous shear layer sources to about  $15u_\tau$  due to the logarithmic region and  $18u_\tau$  due to the

upper channel. The convection velocities from the MS and TT partial pressures for all the regions shows that for the MS partial pressures, the low wavenumbers have the same value as the logarithmic region, but approach the buffer layer curve at the higher wavenumbers. The peak value of  $U_c$  appears to be  $15.3u_\tau$  at  $k_x\delta = 3$ , decreasing to about  $11u_\tau$  at the highest wavenumbers.

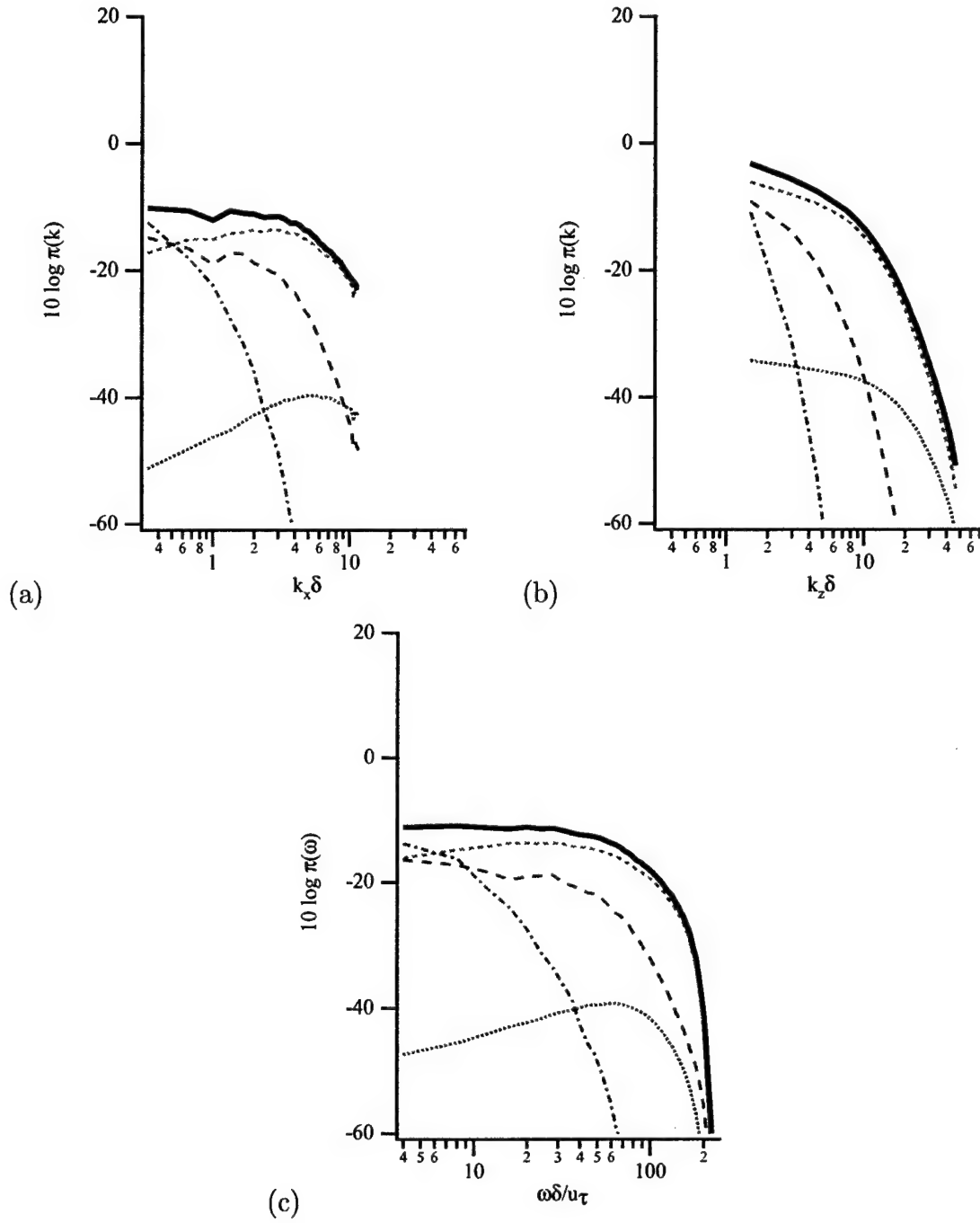


Figure 12. One-dimensional spectra of  $\pi^{MS}$  from LES8; (a) streamwise wavenumber and (b) spanwise wavenumber and (c) frequency; — : all regions (R1234), ..... : viscous shear layer(R1), - · - · - : buffer layer, - - - - : logarithmic region, and - - - : upper channel.

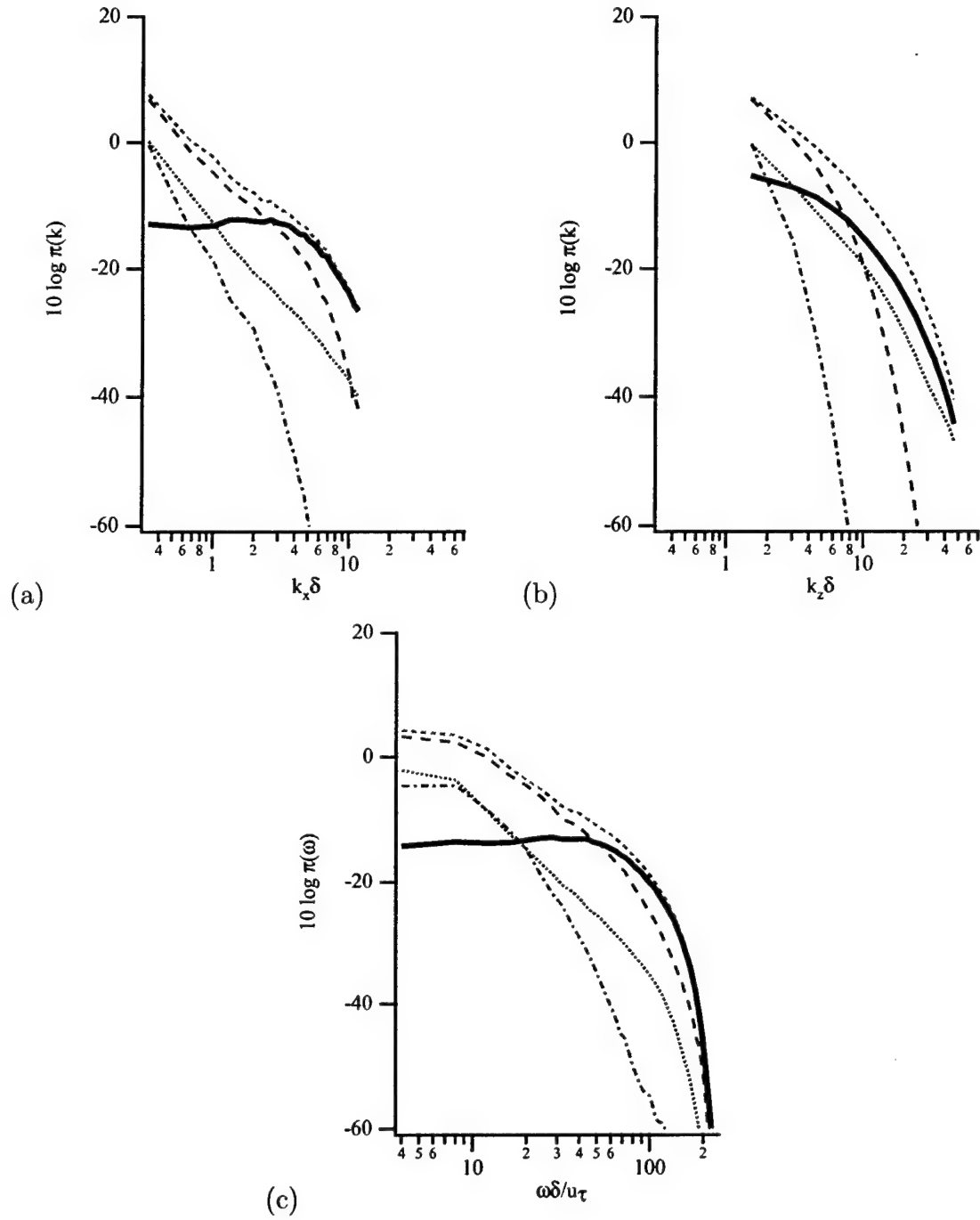


Figure 13. One-dimensional spectra of  $\pi^{TT}$  from LES8 (a) streamwise wavenumber and (b) spanwise wavenumber and (c) frequency. — : all regions (R1234), ..... : viscous shear layer(R1), - · - · - : buffer layer(R2), - - - - : logarithmic region(R3), and - - - : upper channel(R4).



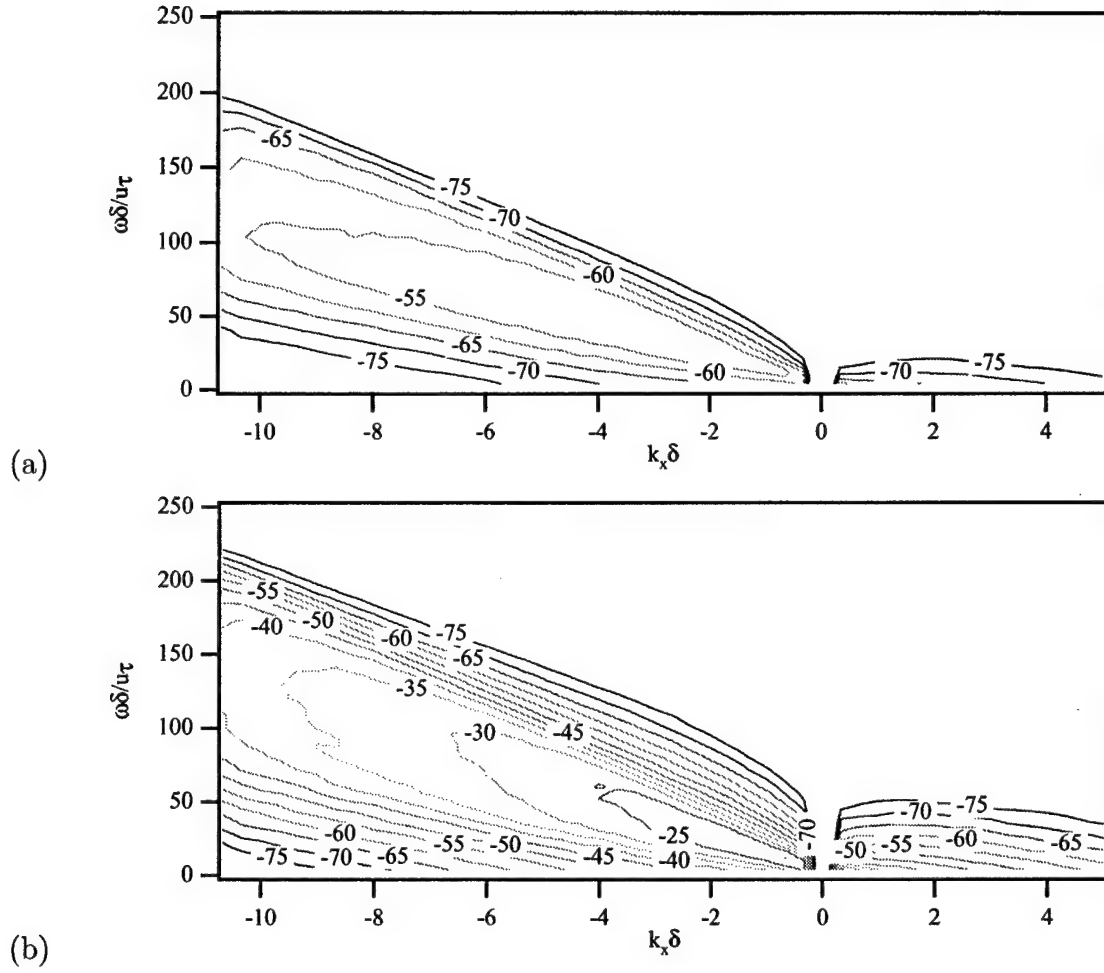


Figure 14. Two-dimensional contour plots of  $k_x - \omega$  spectra of  $\pi^{MS}$  from LES8; (a) viscous shear layer (R1) and (b) buffer layer (R2).

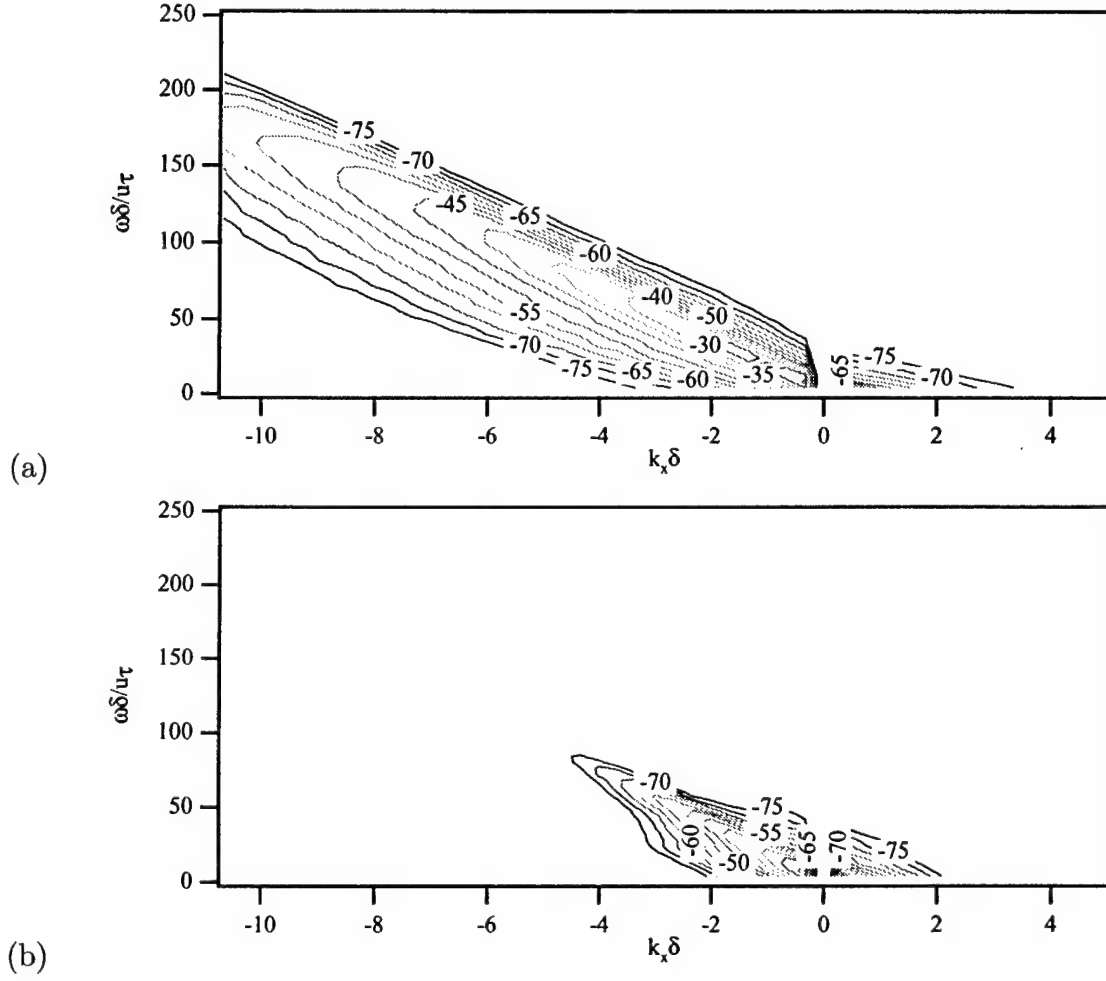


Figure 15. Two-dimensional contour plots of  $k_x - \omega$  spectra of  $\pi^{MS}$  from LES8; (a) logarithmic region (R3) and (b) upper channel (R4).

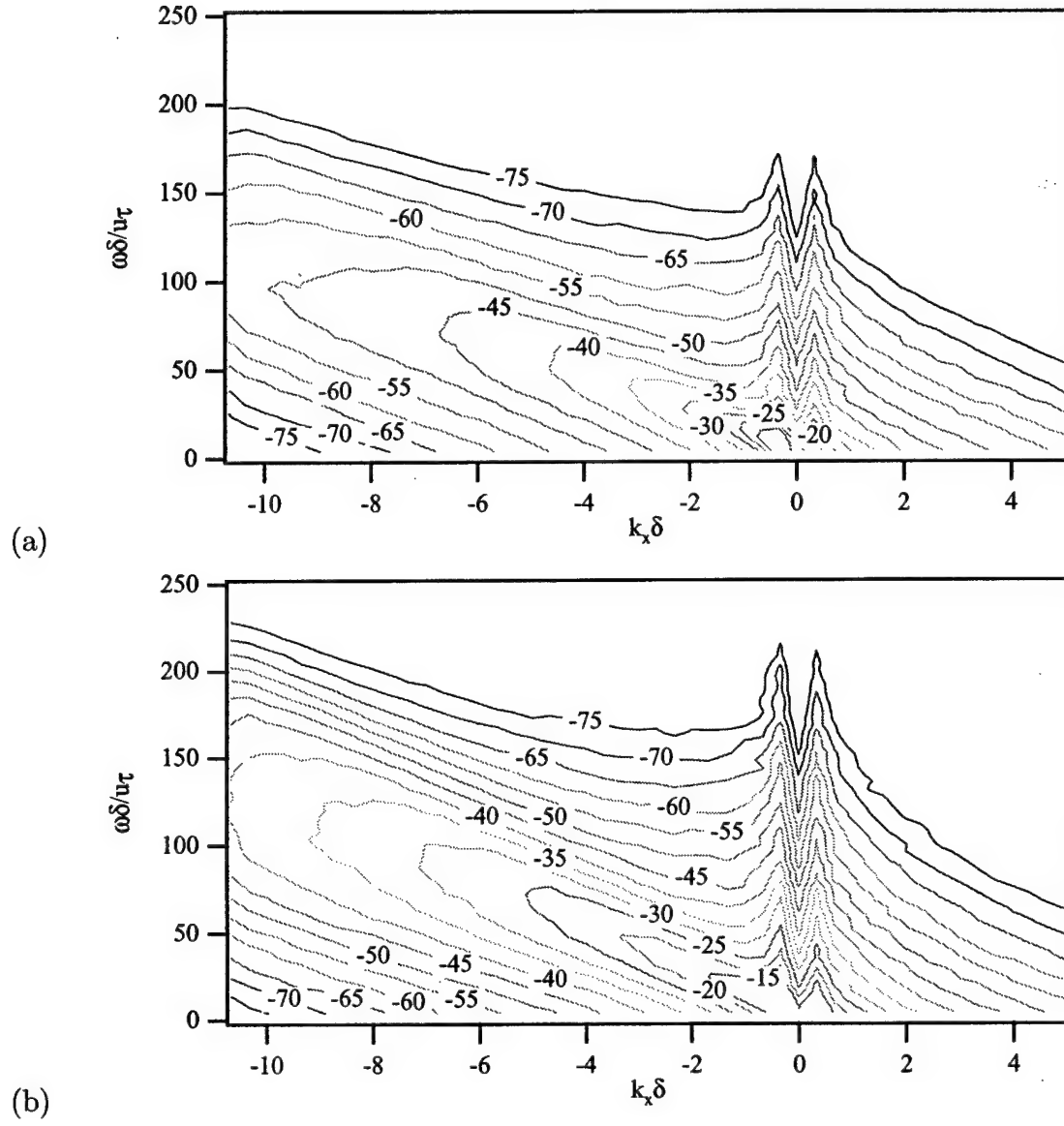


Figure 16. Two-dimensional contour plots of  $k_x - \omega$  spectra of  $\pi^{TT}$  from LES8; (a) viscous shear layer (R1) and (b) buffer layer (R2).

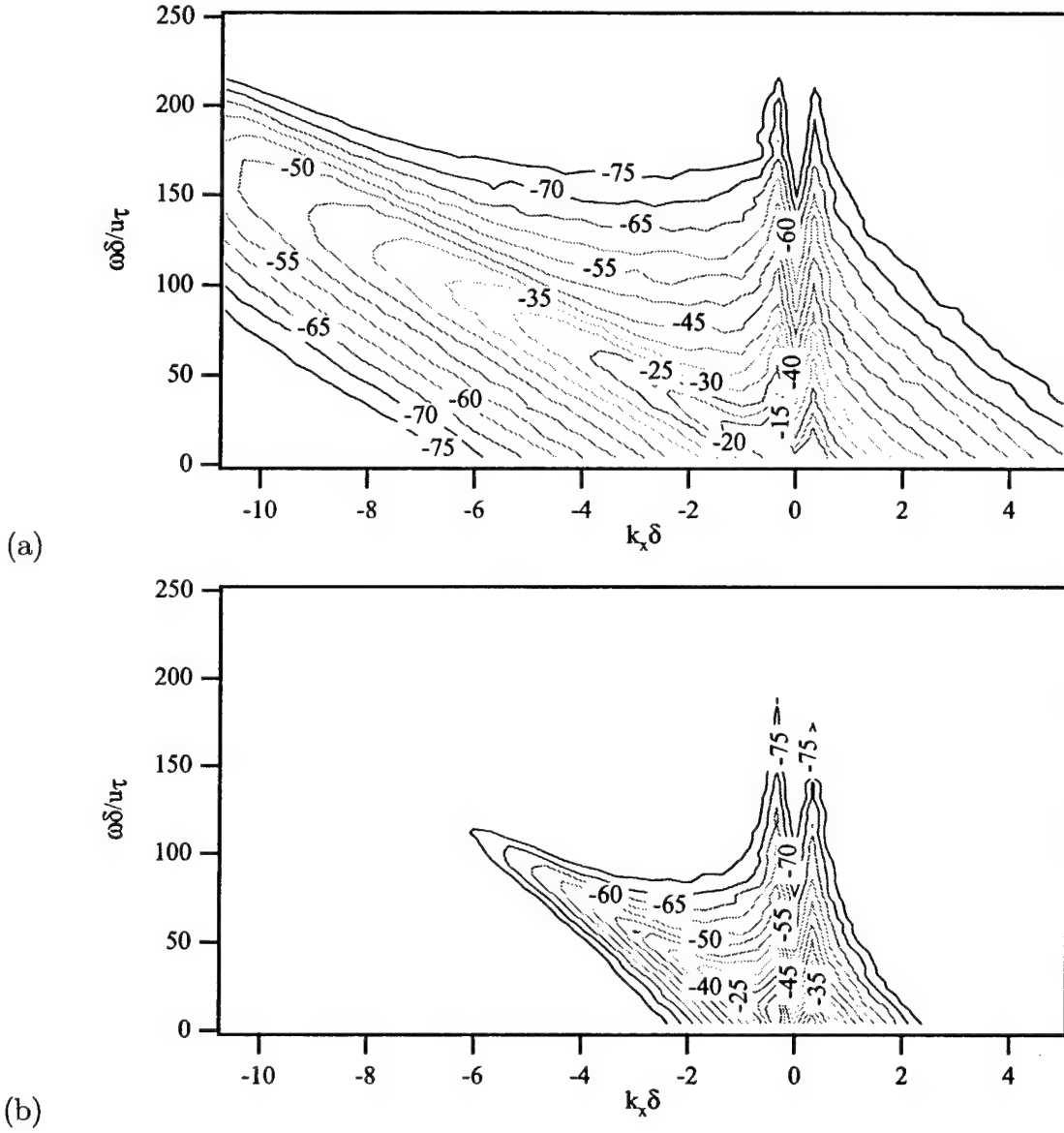


Figure 17. Two-dimensional contour plots of  $k_x - \omega$  spectra of  $\pi^{TT}$  from LES8; (a) logarithmic region (R3) and (b) upper channel (R4).

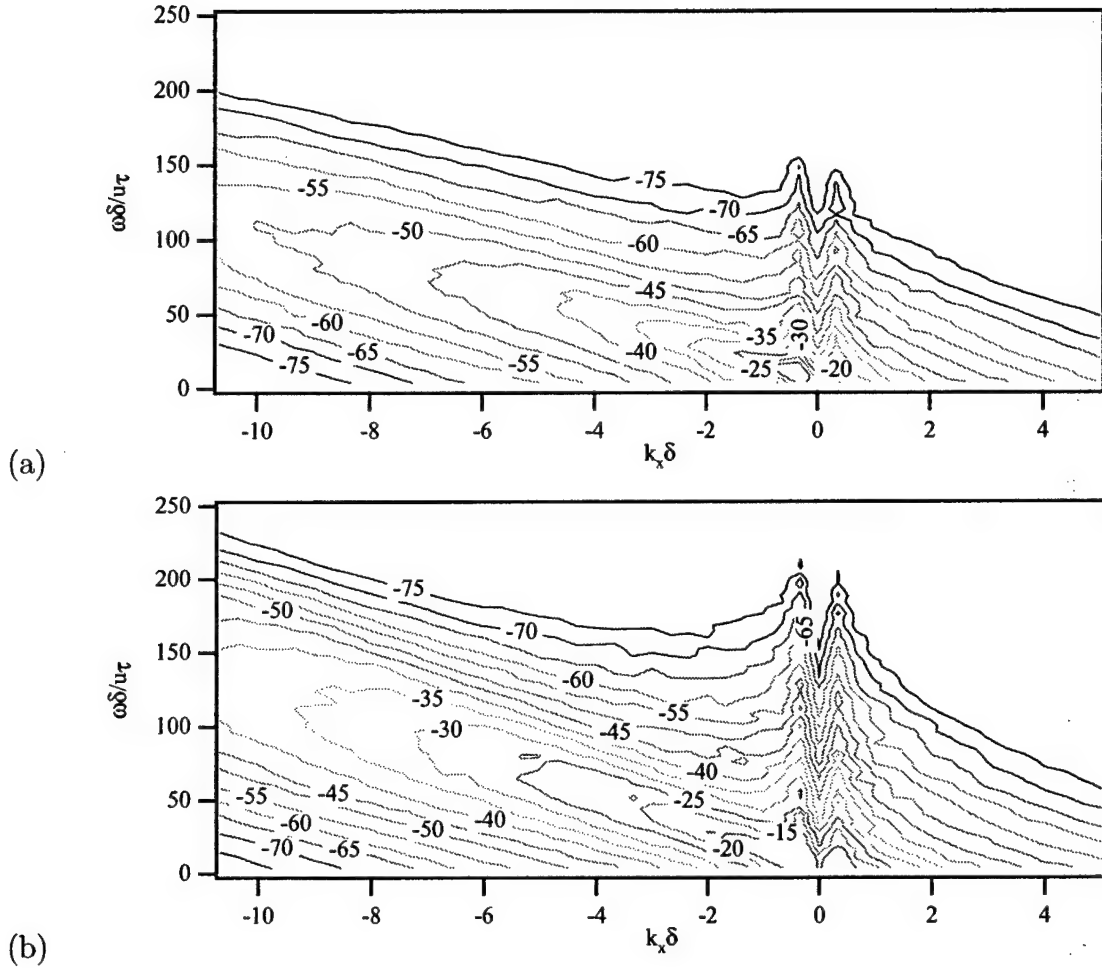


Figure 18. Two-dimensional contour plots of  $k_x - \omega$  spectra of  $\pi^{TT}$  from LES9; (a) viscous shear layer (R1) and (b) buffer layer (R2).

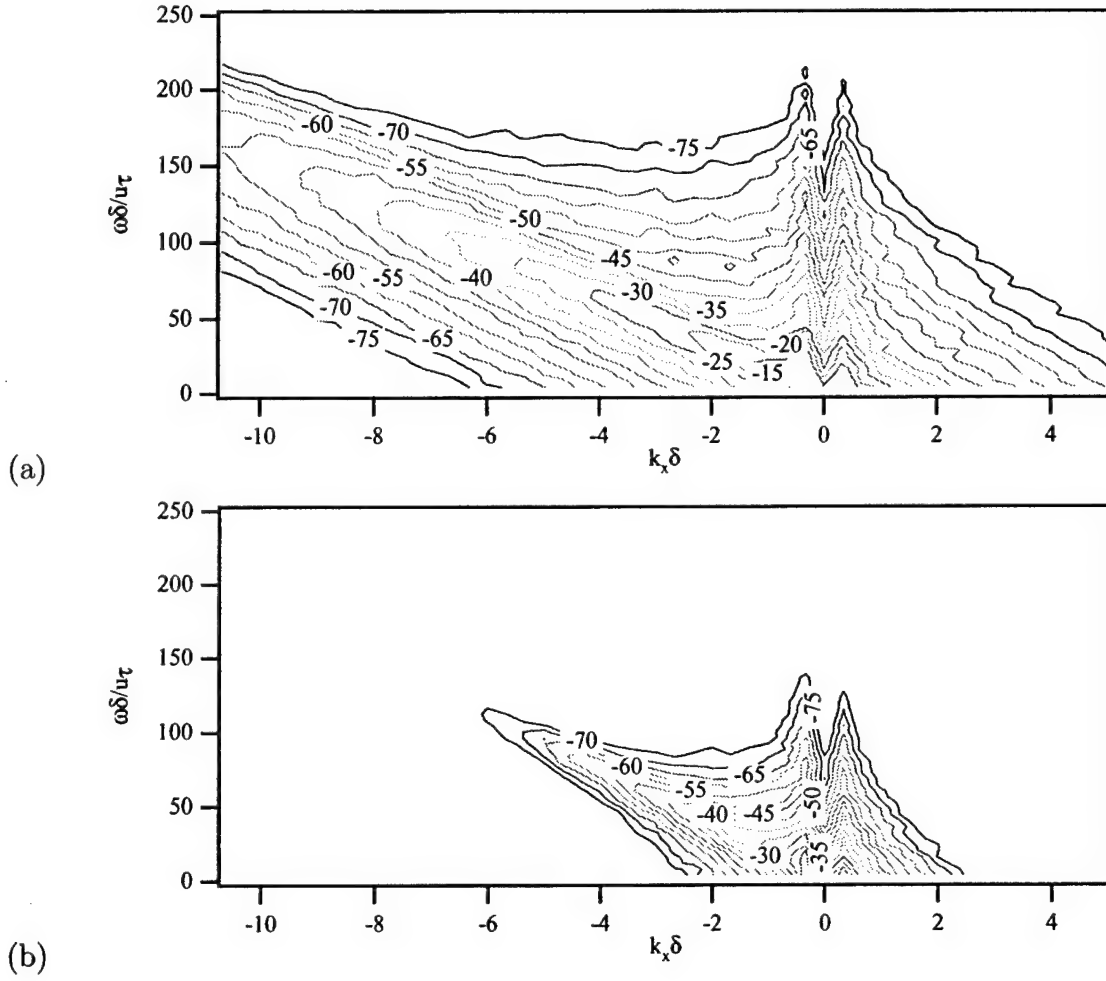


Figure 19. Two-dimensional contour plots of  $k_x - \omega$  spectra of  $\pi^{TT}$  from LES9; (a) logarithmic region (R3) and (b) upper channel (R4).

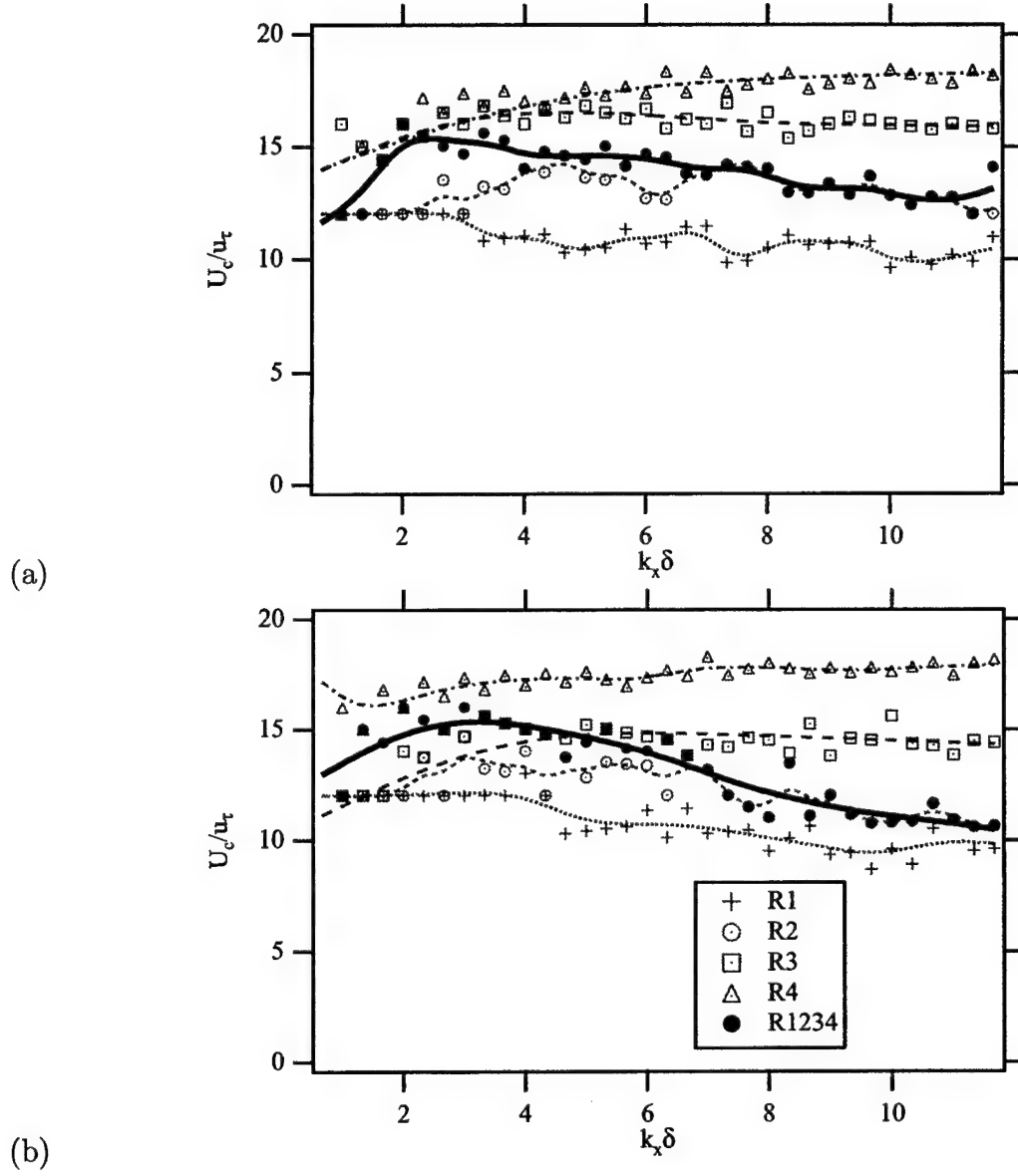


Figure 20. Convection velocities from peak of  $k_x - \omega$  spectra from LES8, (a) MS (b) TT.

### Constant- $\omega$ cuts of $k_x - \omega$ spectra of partial pressures

Constant frequency cuts of the  $k_x - \omega$  spectra for the MS pressures from all the regions compared with that for the individual regions are shown in Figure 21. At the lowest frequency, Figure 21(a), the low- $k_x$  side of the convective ridge seems to be due to the logarithmic region; the peak due to both the buffer layer and logarithmic region; the high- $k_x$  side due to the buffer layer. As frequency increases, Figure 21(b-d), the importance of the logarithmic region diminishes and the buffer layer appears to be primarily responsible for the convective ridge energy. In the two lowest- $\omega$  cases [Figure 21(a-b)] the subconvective range has an approximate  $k_x^2$  behavior. As frequency increases, the subconvective range goes to  $k_x^0$ .

Constant frequency cuts of the  $k_x - \omega$  spectra for the TT pressures from LES8 from all the regions compared with that for the individual regions are shown in Figure 22. Results from LES were almost identical, so are not shown. Similar to the broad-band partial pressures, in the low- $k_x$  the constant- $\omega$  cuts from the individual regions have higher energy than that due to all the regions (R1234). For all the frequencies the lowest- $k_x$  partial pressures from the buffer layer and logarithmic region are essentially equal, diverging as  $k_x$  approaches the convective ridge. This is not surprising, in light of the fact that the one-dimensional broad-band wavenumber spectra for the buffer layer and logarithmic region are very close in the the lowest- $k_x$  (Figure 13). With regards to the partial pressures from the buffer layer and logarithmic region, as frequency increases, the relative level of the pressure in the lowest  $k_x$  decreases with respect to that at the convective ridge; this points out that the low- $k_x$  energy build-up, though evident at all frequencies is mostly concentrated at low- $\omega$ . A feature of the partial pressures from all the regions is that as frequency increases, the minimum between the subconvective and convective ridge peaks becomes more pronounced and move to higher  $k_x$ .

In the low- $\omega$  [Figure 22(a)], the low- $k_x$  side and peak of the convective ridge mimics the behavior of the logarithmic region, while the high- $k_x$  side mimics the pressure from the buffer layer. Note that for part of the high- $k_x$  side of the convective ridge the partial pressure from the buffer layer is actually higher than that from all regions. As frequency increases, the convective ridge partial pressure due to the logarithmic region decreases with respect to that from the buffer layer; thus the buffer layer partial pressure is the dominant source of convective ridge energy there.



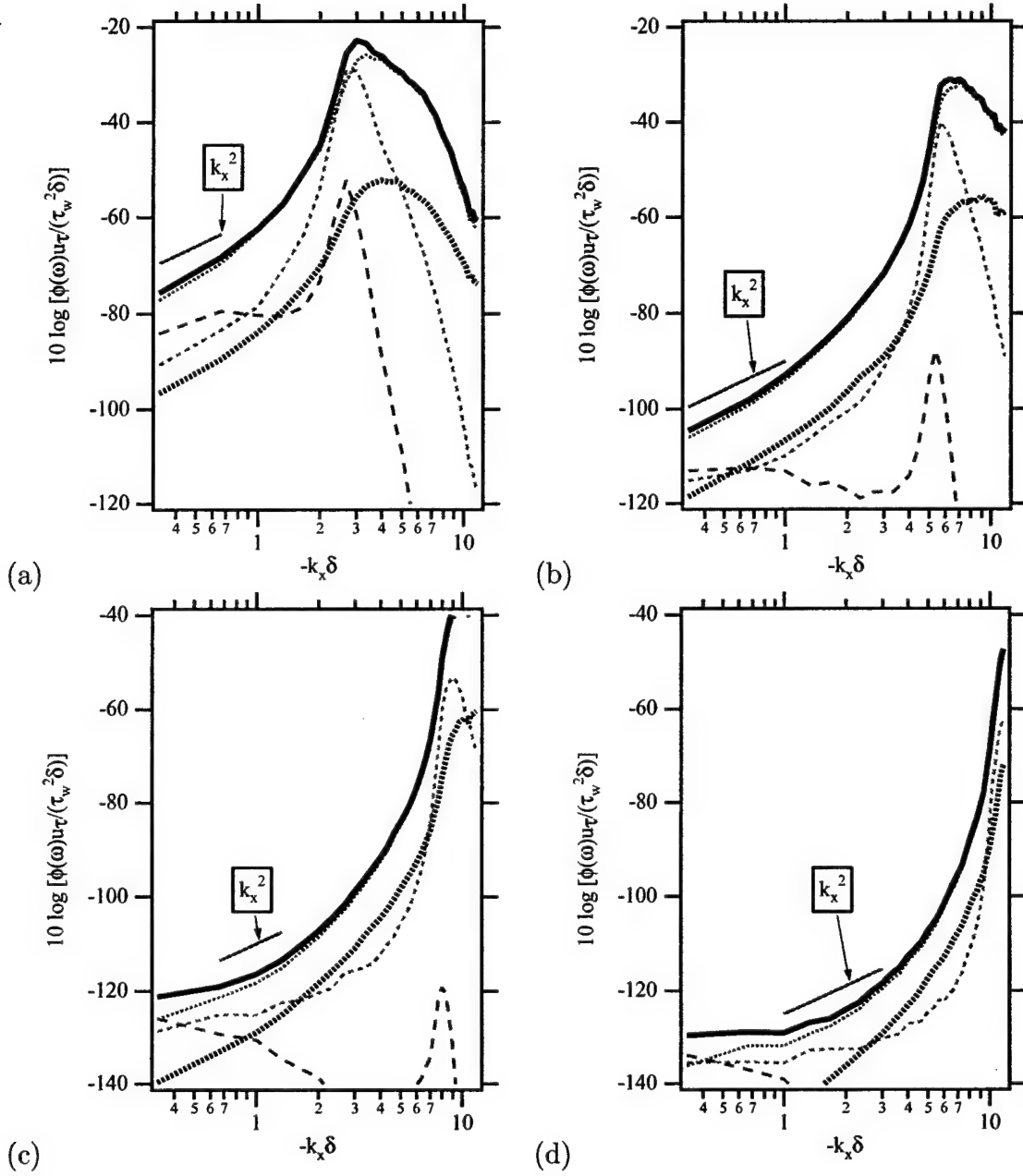


Figure 21. Constant frequency cuts of  $k_x-\omega$  spectra of MS partial pressures from four regions of the channel; (a)  $\omega\delta/u_\tau = 52$  (b)  $\omega\delta/u_\tau = 104$  (c)  $\omega\delta/u_\tau = 156$  and (d)  $\omega\delta/u_\tau = 204$ ; — : R1234; ..... : R1; — · — : R2; - - - - : R3; - - - - : R4.

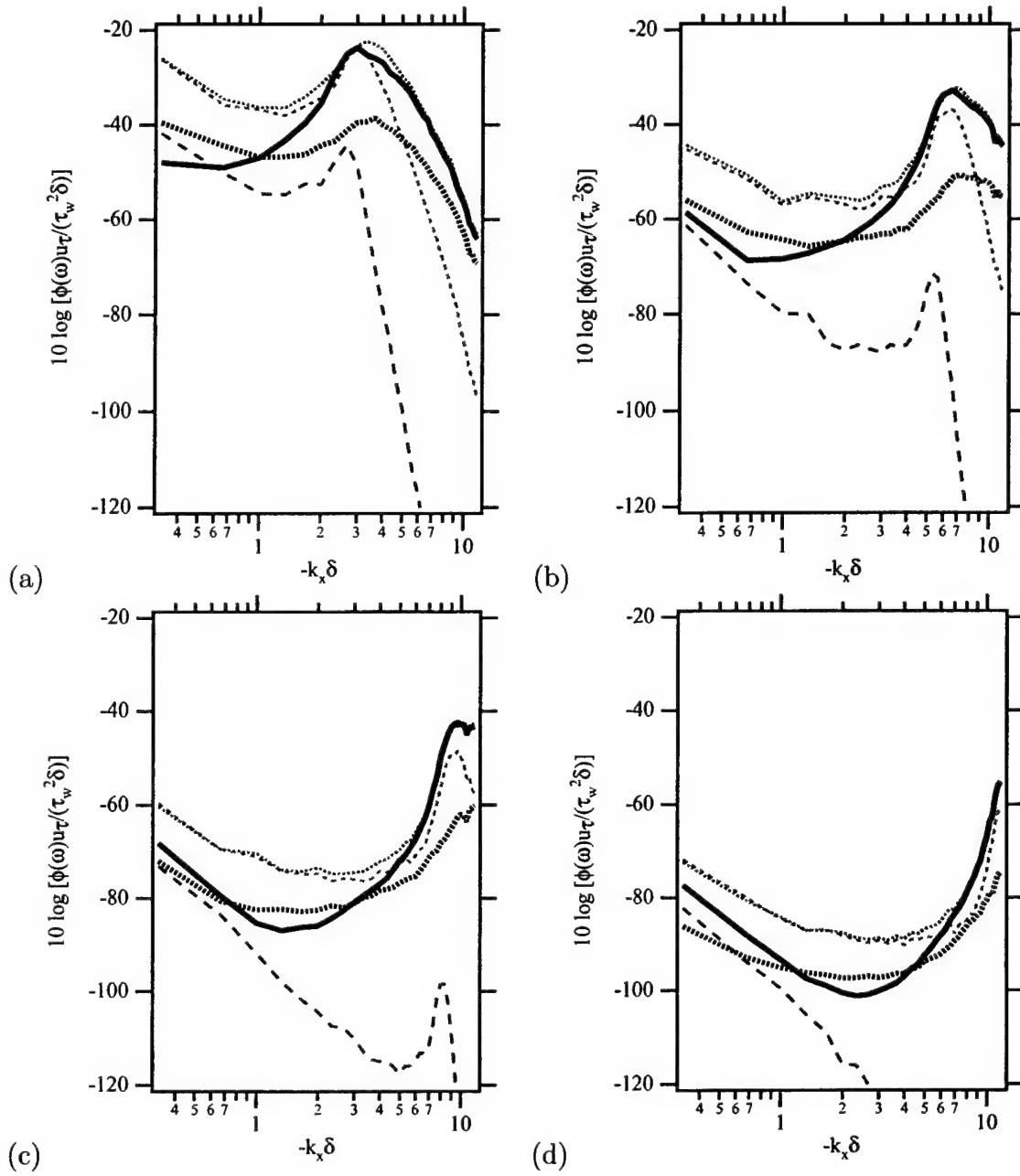


Figure 22. Constant frequency cuts of  $k_x - \omega$  spectra of TT partial pressures from four regions of the channel; (a)  $\omega\delta/u_\tau = 52$  (b)  $\omega\delta/u_\tau = 104$  (c)  $\omega\delta/u_\tau = 156$  and (d)  $\omega\delta/u_\tau = 204$ ; — : R1234; ..... : R1; - · - · - : R2; - - - - : R3; - - - - : R4.

## Comparison to semi-empirical formulations

The incompressible model for the wall-pressure spectra of Chase<sup>15</sup> is given by

$$\Psi_c(\mathbf{K}, \omega) = \frac{\rho^2 u_\tau^3}{[K_+^2 + (b\delta)^{-2}]^{5/2}} \left\{ C_T K^2 \left[ \frac{K_+^2 + (b\delta)^{-2}}{K^2 + (b\delta)^{-2}} \right] + C_M k_x^2 \right\} \quad (23)$$

where

$$K_+^2 \equiv \frac{(\omega - U_c k_x)^2}{(h u_\tau)^2} + K^2 \quad (24)$$

There are four constants that need to be determined:  $C_T$  and  $C_M$ , which determine the amplitude of the TT and MS pressures, respectively,  $b$  and  $h$ . The convection velocity,  $U_c$  determines at which value of  $k_x$  the convective ridge appears. It has been assumed that the pressure source layer is of thickness  $b\delta$ , where  $\delta$  is the boundary layer thickness. (24) takes into account the assumed decorrelation of the velocity-field sources as they convect downstream at  $U_c$ ;  $h u_\tau$  is a characteristic turbulence velocity. The parameter  $h$  controls, to some extent, the width of the convective ridge. Chase<sup>15</sup> recommended that the values  $h = 3$ ,  $C_T h = 0.014$ ,  $C_M h = 0.466$  and  $b = 0.75$  be used.

Figure 23 compares the spectrum of Chase<sup>15</sup> to the total, TT, and MS spectra from LES9 at  $\omega\delta/u_\tau = 156$ . The spectra (23) has been integrated over all  $k_z$  to be consistent with the LES9 results. The results of Chase are shown with parameters which lead to a best fit of the subconvective range and convective ridge—  $h = 1$ ,  $C_T h = 8 \times 10^{-5}$ ,  $C_M h = 5 \times 10^{-2}$  and  $b = 1$ . The model has the correct wavenumber-white [*i.e.*,  $\phi(k_x) \sim k_x^0$ ] behavior in the subconvective range, and, as can be seen in (23) the MS component has a  $k_x^2$  behavior in this range as shown *e.g.*, in Figure 22. The model does not correctly predict the width of the convective ridge— this could be due to fact that it considers only the velocity-field sources in the logarithmic region. As shown in Figure 22 the MS pressure from the logarithmic region is indeed, very narrow-peaked, and the full width of the convective ridge comes from sources in the buffer layer. The rolloff between the convective ridge and subconvective range is determined primarily by the values of  $C_M$  and  $C_T$ , and, as constants, they cannot reflect the fact that the rolloff varies with  $\omega$  as shown in Figure 22.

## CONCLUSIONS

It was found that the form of the nonlinear terms makes a difference in the TT pressure for the entire channel in the subconvective wavenumber range. With the rotational form (LES8), the subconvective pressures have high energy build-up in the lowest wavenumbers, whereas with the skew-symmetric form (LES9), there is no such behavior. When the subconvective pressures are decomposed into those from the four regions of the channel, the effect of advective scheme is not apparent: the form of the nonlinear terms only affects the pressure over the entire channel.

It was shown that the TT pressure is exclusively responsible for the subconvective pressure and that both the buffer layer and logarithmic region are the main contributors. The MS pressure behaves as  $k_x^2$ , thus going to zero as  $k_x \rightarrow 0$ .

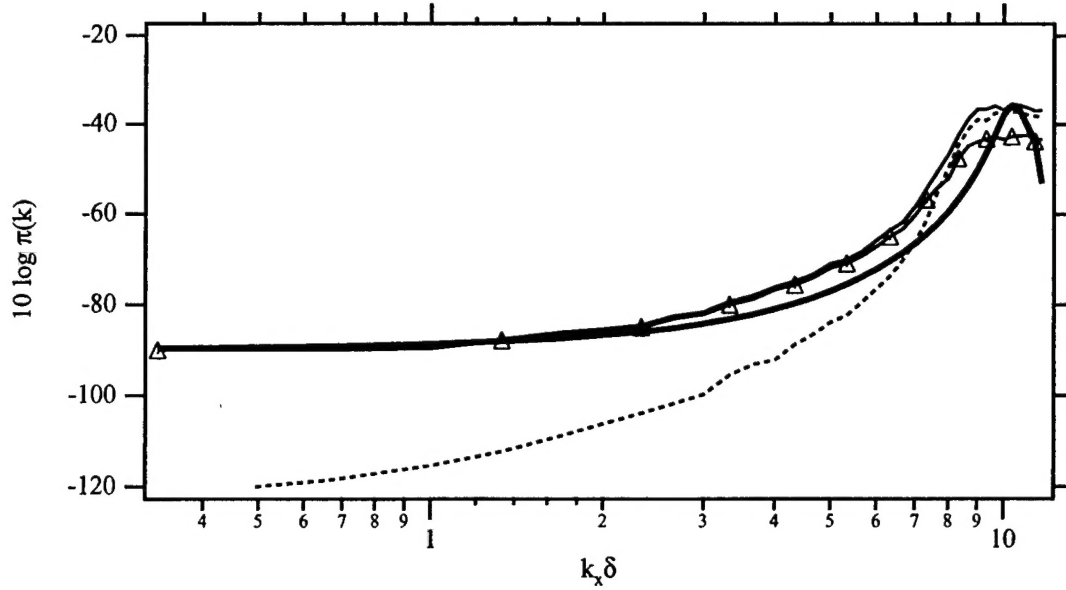


Figure 23. Constant frequency cuts of  $k_x - \omega$  spectra at  $\omega\delta/u_\tau = 156$  compared with Chase<sup>15</sup>; — : Chase; — : total; ..... : MS;  $\Delta$  : TT.

With regards to the pressures at the convective ridge, the one-dimensional broadband spectra shows that the MS pressure is dominant in the low- to medium-wavenumbers and frequencies, but in the higher wavenumbers the TT pressure becomes dominant. Constant frequency slices of the two-dimensional  $k_x - \omega$  spectra shows that in the lower frequencies both the logarithmic region and buffer layer are responsible for the MS convective pressures, but as frequency increase, the buffer layer becomes more dominant. The same is true for the TT pressure.

Spectra predicted with the semi-empirical model of Chase<sup>15</sup> was compared with LES results. It is apparent that such models can be tuned to have the correct behavior in the subconvective range and height of the convective ridge. However, possibly due to lack of inclusion of buffer layer sources, the width of the convective ridge is underpredicted. Also, such a model cannot describe the frequency-dependent rolloff between the convective ridge and subconvective wavenumber range. Parameterization of the buffer layer sources is necessary for a fully-successful wall-pressure model.

## REFERENCES

1. Peter A. Chang, Ugo Piomelli, and William Blake. Relationship between wall pressure and velocity field sources. *Physics of Fluids - A*, 11(11), 1999.
2. Peter A. Chang. *Relationships between wall pressure and velocity field sources*. Phd, Univ of Maryland, 1998.
3. T.A. Zang. On the rotational and skew-symmetric forms for incompressible flow simulations. *Appl. Num. Math.*, 7(27), 1991.
4. John Kim, Parviz Moin, and Robert Moser. Turbulence statistics in fully developed channel flow at low reynolds number. *Journal of Fluid Mechanics*, 177:133–166, 1987.
5. Hancheon Choi and Parviz Moin. On the space-time characteristics of wall pressure fluctuations. *Physics of Fluids A*, 8:1450–1460, 1990.
6. D.E. Newland. *An introduction to Random Vibrations and Spectral Analysis*. Longman, New York, 2nd edition, 1984.
7. P.A. Chang, B.M. Abraham, and U. Piomelli. Wavenumber-frequency characteristics of wall pressure fluctuations computed using turbulence simulations. In K.W. Wang, A.H. von Flotow, R. Soureshi, E.W. Hendricks, and T.M. Farabee, editors, *1994 ASME International Mechanical Engineering Congress and Exposition, Symposium on Active Control of Vibration and Noise*, volume DE-Vol. 75, pages 229–244, Chicago, IL, 1994.
8. William L. Keith, D.A. Hurdis, and B.M. Abraham. A comparison of turbulent boundary layer wall-pressure spectra. *Journal of Fluids Engineering*, 114:338–347, 1992.
9. H. Kreplin and H. Eckelmann. Behavior of the three fluctuating velocity components in the wall region of a turbulent channel flow. *Physics of Fluids*, 22, 1979.
10. Arne V. Johansson, Jen-Yuan Her, and Joseph H. Haritonidis. On the generation of high-amplitude wall-pressure peaks in turbulent boundary layers and spots. *Journal of Fluid Mechanics*, 175:119–142, 1987.
11. Bart A. Singer. Large-eddy simulation of turbulent wall-pressure fluctuations. Technical Report CR-198276, NASA, 1996.
12. Theodore M. Farabee and M.J. Casarella. Spectral features of wall pressure fluctuations beneath turbulent boundary layers. *Physics of Fluids - A*, 3(10):2410–2420, 1991.
13. S.P. Gravante, A.M. Naguib, C.E. Wark, and H.M. Nagib. Characterization of the pressure fluctuations under a fully developed turbulent boundary layer. *AIAA Journal*, 36(10):1808–1816, 1998.

14. P. Bradshaw. Inactive motions and pressure fluctuations in turbulent boundary layers. *Journal of Fluid Mechanics*, 30(2):241–258, 1967.
15. D.M. Chase. The character of the turbulent wall pressure spectrum at subconvective wavenumbers and a suggested comprehensive model. *Journal of Sound and Vibration*, 112(1):125–147, 1987.

## DISTRIBUTION

### Copies

#### ONR

1	333	L.P. Purtell
1	333	K.H. Kim

#### DTIC

1

#### DIVISION DISTRIBUTION

1	0112	J. Barkyoumb
1	3442	TIC
10	5060	
1	5200	R. Stenson
1	5200	G. Karafiath
5	5200	P. Chang
1	5200	W. Wilson
1	5400	J. Gorski
1	5400	Y.T Lee
1	5500	F. Noblesse
1	705	W. Blake
1	725	I. Zawadzki
1	725	T. Farabee